ACS APPLIED ENERGY MATERIALS

www.acsaem.org Article

Impact of Multivalent Cations on Interfacial Layering in Water-In-Salt Electrolytes

Alexis G. Hoane, Qianlu Zheng, Nicholas D. Maldonado, Rosa M. Espinosa-Marzal, and Andrew A. Gewirth*

Cite This: https://doi.org/10.1021/acsaem.4c00507 Read Online

ACCESS | Metrics & More | Article Recommendations | Supporting Information

ABSTRACT: Water-in-salt electrolytes (WiSEs) are of interest for use as aqueous multivalent electrolytes due to their potential to address reversibility and passivation concerns common in multivalent batteries. In this work, the impact of the addition of multivalent cation salts, including $Zn(TFSI)_2$, $Mg(TFSI)_2$, $Ca(TFSI)_2$, and $Al(TFSI)_3$ on the double layer behavior in LiTFSI WiSE is investigated. Surface-enhanced infrared absorption spectroscopy (SEIRAS) is utilized to observe the potential-dependent double-layer composition. $TFSI^-$ is enriched at relatively positive potentials for LiTFSI WiSE, and water is enriched at negative potentials for mixed electrolytes containing Mg^{2+} and Ca^{2+}, but this shift does not hold for mixed electrolytes containing Zn^{2+} or Al^{3+}. Ultramicroelectrode (UME) voltammetry shows confinement of a probe molecule $Fe(CN)_6^{4-}$ at the interphase in the presence of Mg^{2+} and Ca^{2+}, an effect that is eliminated by the addition of 1.75 and 1.25 mM of Zn^{2+} or Al^{3+}, respectively, to LiTFSI WiSE. Atomic force microscope (AFM) measurements show the presence of smaller interlayer distances at positive potentials relative to those seen without the presence of Zn^{2+}. These effects are correlated to cation pK_a, highlighting the importance of the water structure at the interphase of WiSE for multivalent electrolytes.

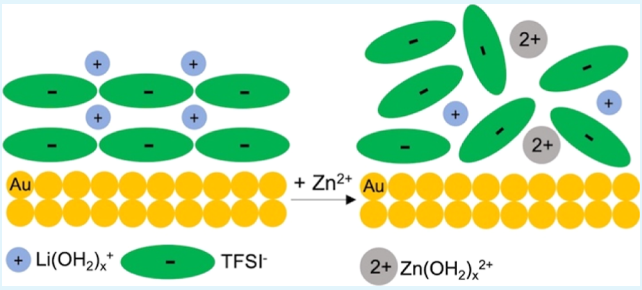

KEYWORDS: *water-in-salt electrolyte, multivalent metal-ion batteries, double-layer, ATR-SEIRAS, atomic force microscopy*

1. INTRODUCTION

The development of high-performance batteries forms an intense focus of study due to their utility in renewable and sustainable energy schemes.[1] Li−ion batteries are particularly useful among available battery chemistries due to their high energy density, resiliency to fast charging rates, and long cycle life.[1,2] Nonetheless, Li−ion battery capacities have plateaued over the past decade as these capacities approach theoretical limits.[3] Additionally, limitations in the availability of raw materials used in many Li−ion batteries, including cobalt and Li, present roadblocks for the future widespread adoption of Li−ion batteries.[3]

Substantial effort has been expended to develop alternative battery chemistries to circumvent these barriers. Multivalent batteries featuring the use of Zn, Mg, Ca, or Al have all been considered.[4] Zn−ion batteries composed of a Zn metal anode and Zn^{2+} intercalation cathode are considered a viable option due to the considerable volumetric capacity of the Zn metal anode (5851 mAh cm^{-3}), relative environmental abundance of raw materials, and low material and assembly costs compared to competitors.[5,6] Further, the Zn−ion battery may be more tractable than other multivalent batteries (Mg, Ca, and Al) at both the anode and cathode sides. Zn^{2+} forms a relatively lower hydrated radius, favorable for ion intercalation into a cathode, and Zn−ion batteries exhibit a lower propensity to form a dense passivation layer at the anode.[6] However, multivalent cation batteries also face significant challenges that present opportunities for improvement. The high desolvation penalty due to multivalency increases cell resistance,[5] while the formation of dendrites at the anode limits Coulombic efficiency and cycle life, and the hydrogen evolution reaction (HER) causes solvent loss and passivation of the anode.[6] The use of nonaqueous solvents may weaken the impact of these issues, but water-based electrolytes are preferred due to the inherent safety and low cost of water as a solvent.

One emerging way to circumvent electrolyte issues in multivalent batteries is by employing highly concentrated water-in-salt electrolytes (WiSEs).[7] WiSE composed of bis(trifluoromethanesulfonyl)imide ($TFSI^-$) salts were initially used in a Li−ion battery[8] and have subsequently garnered substantial attention.[9−14] WiSE exhibits several interesting properties.[15] The bulk solvation structure inhibits HER and expands the electrochemical stability window by reducing

Received: March 1, 2024
Revised: May 16, 2024
Accepted: May 21, 2024

water activity due to coordination with a cation.[8] An unusually high transference number is observed considering the electrolyte's high viscosity, thought to be due to the formation of water-rich channels that allow for the transportation of Li^+ due to the heterogeneous bulk structure of the electrolyte.[16−18] Our previous work[11,12] observed a potential-dependent layered structure in LiTFSI WiSE at the interphase. Atomic force microscopy (AFM), potential-dependent spectroscopy, and electrochemical experiments revealed that while hydrated Li species were dominant when a negative potential was applied to a metal surface, they were displaced by $TFSI^-$ and higher order clusters consisting of $[Li(H_2O)_x]^+([TFSI]^-)_y$ at more positive potentials. These structures may further stabilize the interphase via solvent exclusion.

The use of a mixed 20 m LiTFSI + 1 m $Zn(TFSI)_2$ WiSE suggested that the WiSE might be an effective strategy to mitigate the challenges of single cation electrolytes in multivalent batteries.[19] The authors found that the electrolyte effectively inhibited the HER, enabling reversible plating of Zn and inhibiting dendrite formation. Subsequent investigation of this electrolyte[20] indicated that, even at WiSE concentrations, the solvation structure of Zn^{2+} consists almost exclusively of water molecules in the bulk electrolyte. The hydrated Zn^{2+} stands in contrast to the environment around Li^+, which features both $TFSI^-$ and water coordination.[8] This contrast suggests that the structure of the Li WiSE and the Li + Zn WiSE must also be different at the interphase,[20] but little work attends to this area. Beyond this, any further differences in electrolytes formed from Li WiSE and other multivalent cations remain unexplored.

Ultramicroelectrodes (UMEs) are utilized to study redox processes in battery electrolytes.[21,22] UMEs feature the presence of spherical diffusion, which is particularly beneficial in less conductive electrolytes. Interactions between a probe redox species and the surrounding electrolyte impact voltammetry, thus revealing information about the solvation environment at the interphase.[11]

Attenuated total reflectance surface-enhanced infrared absorption spectroscopy (ATR-SEIRAS)[23] can be utilized to probe potential-dependent changes in abundance and orientation of molecules at a metal surface.[23−25] ATR-SEIRAS employs backside illumination of the electrode, which does not require light to travel through a concentrated electrolyte, obviating the need for a possibly detrimental thin layer cell needed to transmit light to the front side of an electrode.[24] Alternatively, ATR-SIERAS requires the use of roughened electrodes of uncertain orientation. Prior research has used SEIRAS to observe the potential-dependent changes to the electrochemical double layer of WiSEs.[11,26] However, the effect of multivalent anion addition on the WiSE interphase has not been reported.

AFM is also used to study potential-dependent EDL structure in highly concentrated electrolytes or ionic liquids.[11,27] Here, AFM force curves are used to analyze the effect of multivalent cations on the layering and ordered structures in the WiSE interphase.

In this work, UME voltammetry, ATR-SEIRAS, and AFM force curves are used to investigate the composition of the solid/WiSE interphase and examine how this composition is altered through the addition of multivalent cations. We focus initially on the effect of Zn^{2+} and then further investigate the effect of the addition of Mg^{2+}, Ca^{2+}, and Al^{3+}. Results indicate that the addition of Zn^{2+} and Al^{3+} to the LiTFSI WiSE disrupts the ordered, layered, and potential-dependent structure of the LiTFSI WiSE interphase as previously established,[11,12] while Mg^{2+} and Ca^{2+} do not. This effect is explained by invoking cation pK_a as a reporter of the strength of water association with the foreign cations.

2. EXPERIMENTAL SECTION

2.1. Electrolyte Preparation. Lithium bis(trifluoromethane sulfonyl) imide (LiTFSI, 99.95%, Sigma-Aldrich), magnesium bis(trifluoromethane sulfonyl) imide ($Mg(TFSI)_2$, 99.5%, Solvionic), calcium bis(trifluoromethane sulfonyl) imide ($Ca(TFSI)_2$, 99.5%, Solvionic), and sodium bis(trifluoromethane sulfonyl imide) (NaTFSI, 99.5%, Solvionic) were dried on a Schlenk line at 120 °C under vacuum for 12 h and stored in an Ar-filled glovebox (<1 ppm of O_2 and <1 ppm of H_2O).

Aqueous solutions of 20 m LiTFSI and 20 m LiTFSI + 1 m $Zn(TFSI)_2$, 1 m $Ca(TFSI)_2$, and 0.5 m $Mg(TFSI)_2$, were prepared by dissolving salt in Milli-Q water (18.2 MΩ cm^{-1}). An aqueous solution of 15 m LiTFSI + 0.1 m $Al(TFSI)_3$ was prepared similarly. Five mM potassium ferricyanide ($K_3Fe(CN)_6$, >99%, Sigma-Aldrich) + 9 m LiTFSI solutions were prepared by mixing 20 m LiTFSI with 20 mM $K_3Fe(CN)_6$ in a 1:3 volume ratio. Five mM $K_3Fe(CN)_6$ + 9 m LiTFSI + x mM $Zn(TFSI)_2$, $Ca(TFSI)_2$, $Mg(TFSI)_2$, or $Al(TFSI)_3$ solutions were prepared by adding an aliquot of a concentrated solution of 5 mM K_3FeCN_4 + 9 m LiTFSI + 100x mM $Zn(TFSI)_2$, $Ca(TFSI)_2$, $Mg(TFSI)_2$, NaTFSI, or $Al(TFSI)_3$ to the 5 mM $K_3Fe(CN)_6$ + LiTFSI solution.

2.2. Synthesis of $Al(TFSI)_3$. Aluminum bis(trifluoromethane sulfonyl) imide ($Al(TFSI)_3$) was synthesized according to a published procedure.[28] 4 g of bis(trifluoromethane sulfonyl) amide (H-TFSI, >95%, Sigma-Aldrich) was dissolved in 6 mL of Milli-Q water (18.2 MΩ cm^{-1}) along with 6 g of Al foil (Aldrich, 0.5 mm thickness, 99.999%). The reaction vessel was heated at reflux for 24 h. Residual Al was filtered off, and the remaining solution was concentrated with a rotary evaporator and then dried in a vacuum oven at 120 °C and 635 mmHg (281A, Fisherbrand). The resulting product, a white solid, was verified by electrospray ionization (ESI) mass spectrometry with a time-of-flight mass analyzer (Q-TOF Ultima, Waters) and by NMR (Carver B500, Bruker), as shown in Figure S1. All NMR spectra were recorded at 500 MHz. Mass $TFSI^-$ calculated: 280.2 g mol^{-1}, measured: 280.3 m/z.

2.3. Electrochemical Characterization. Electrochemical measurements were performed using a CHI 760D potentiostat. A Pt UME (10 μm diameter, CHI) was used as the working electrode; a Au wire was the counter electrode; and a Ag/AgCl/3 M KCl electrode was the reference. The Pt UME was polished mechanically on a MicroCloth polishing pad (Buehler) using, successively, 3.0, 1.0, 0.25, and 0.05 μm MetaDi Monocrystalline Diamond Suspension (Buehler) and rinsed with Milli-Q water and sonicated for 5 min between each polishing step. The Pt UME was then polished electrochemically in 0.1 M HNO_3 via cyclic voltammetry from 2.0 to −0.5 V vs Ag/AgCl for 20 cycles at 0.05 V/s. UME CV curves were simulated with COMSOL Multiphysics 5.4 software (COMSOL, Inc., Burlington, MA, USA) using the simulation procedures previously described.[22]

2.4. Attenuated Total Reflectance Surface-Enhanced Infrared Spectroscopy (ATR-SEIRAS). ATR-SEIRAS was conducted using either a Nicolet Magna 550 FT-IR spectrometer or a PerkinElmer Spectrum 3 FT-IR spectrometer equipped with a Pike Technologies variable angle VeeMAX III ATR accessory set to a 35° angle of incidence and an in-house fabricated spectroelectrochemical cell based on the previous design.[25] A μ-groove Si wafer (IRUBIS GmbH) was used as the internal reflectance element.[29] The Si wafer was polished mechanically on a MicroCloth polishing pad (Buehler) using, successively, 3.0 and 0.25 μm MetaDi Monocrystalline Diamond Suspension (Buehler), rinsed, and sonicated in Milli-Q water for 15 min between and after polishing steps. The Si wafer was dried under N_2, and a 20 nm thick Au film was evaporated on it at a deposition rate of 0.01 nm/s with a Temescal E-beam evaporator. The Si wafer with 20 nm Au film was then assembled in the ATR-SEIRAS

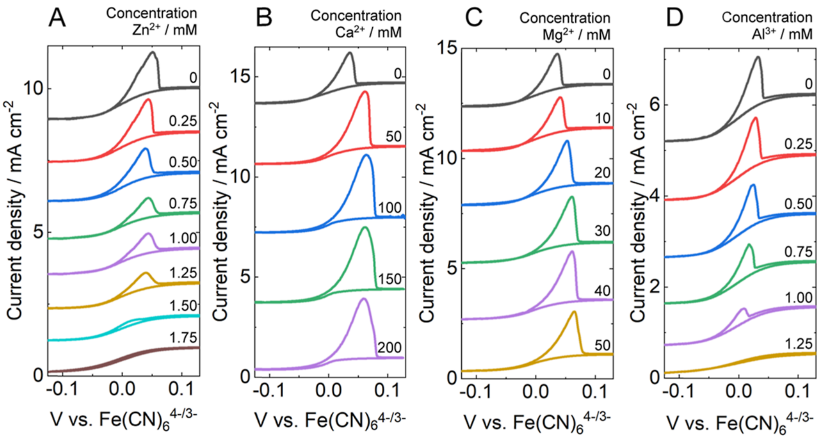

Figure 1. Cyclic voltammograms obtained from a 10 μm Pt UME in a solution containing 5 mM $K_3[Fe(CN)_6]$ and 9 m LiTFSI with additional (A) 0−1.75 mM $Zn(TFSI)_2$, (B) 0−200 mM $Ca(TFSI)_2$, (C) 0−50 mM $Mg(TFSI)_2$, and (D) 0−1.25 mM $Al(TFSI)_3$.

cell and cleaned and conditioned via cyclic voltammetry between −0.5 and 0.9 V vs Ag/Ag$^+$ for 20 cycles at 50 mV/s with the Au-plated Si wafer as the working electrode, Au wire as the counter electrode, and Ag wire as the reference electrode.[25] The Au surface was used as the working electrode for all of the experiments. Potential-dependent spectra were collected using a Au counter and Ag quasireference electrode by using a 70 s potential hold followed by a 0.2 V step between −0.69 and 0.61 V vs Ag/Ag$^+$ for all electrolytes except for 20 m LiTFSI + 1 m $Zn(TFSI)_2$, which was collected using a Zn counter and reference electrodes between 0.1 and 1.4 V vs Zn/Zn^{2+}. All potentials were reported vs Ag/Ag$^+$ except where specified.

2.5. Atomic Force Microscopy (AFM). Force−distance curves were measured by an atomic force microscope (AFM, JPK Nanowizard, Bruker, CA). Silicon AFM probes with a cantilever spring constant of ~0.6 N m^{-1} and a nominal tip radius of ~10 nm were used to probe the electrode−electrolyte interface. The Au substrates were prepared by E-beam evaporation (Temescal FC-2000) of 100 nm thick Au film at a deposition rate of 0.5 nm s^{-1} onto freshly cleaved mica surfaces, and then cleaned and flame-annealed according to a published procedure.[30] This deposition led to a surface roughness of 0.1−0.2 nm RMS within an area of 50 nm × 50 nm, where the measurements were taken. The electrochemical cell was located on the AFM stage with Au-coated mica as the working electrode. In the case of 20 m LiTFSI + 1 m $Zn(TFSI)_2$, Zn wires were used as counter and reference electrodes. For the other electrolytes, a Au wire was used as a counter electrode, and a Ag wire was used as a quasi-reference electrode. A CHI700E potentiostat was used to control the potential. The cell was covered with a Teflon membrane to minimize the exchange of water between the electrolyte solution and ambient air. The system was equilibrated for 20 min before force measurements at the OCP or after applying a bias potential. A total of 64 force−separation curves were measured at each potential with 8 × 8 force mapping within a clean and smooth area of 50 nm × 50 nm. Note that the hard wall is defined at a maximum applied force of 10 nN, which is taken as the zero separation between the tip and surface.

When the tip pushes through a layer of ions, a step or discontinuity appears in the force−distance curve, with the width of the step being the layer thickness ($\Delta = D_1 - D_2$), i.e., the difference between the onset and end separation of each step, D_1 and D_2, respectively.[31] The layer thickness, onset position, and rupture force (F) were determined for all steps resolved on the force−separation profiles. Scatter plots of layer thickness vs layer onset position and layer force vs layer thickness were constructed for each force map to identify the superposition of layers from the clustering of data points. The results were displayed in bubble diagrams, with bubble size being proportional to the frequency (or probability) of each layer measured in a force map (64 force curves).

3. RESULTS

3.1. UME Results. Figure 1A reports CVs obtained from a 10 μm Pt UME in 5 mM $K_3Fe(CN)_6$ and 9 m LiTFSI as a function of added $Zn(TFSI)_2$. The gray, topmost CV of Figure 1A was taken from the electrolyte without $Zn(TFSI)_2$ and exhibits the well-known sigmoidal shape associated with $Fe(CN)_6^{4-}$ oxidation to $Fe(CN)_6^{3-}$ and then reduction back to $Fe(CN)_6^{4-}$.[32] This Zn-free CV also exhibits a peak on the reverse anodic scan between 0.00 and 0.05 V. Such peaks have been observed in the presence of adsorbed or interfacial confined redox species in steady-state systems.[33−35] We attribute this peak to the early oxidation of adsorbed or interfacial confined $Fe(CN)_6^{4-}$ associated with the presence of the high-concentration electrolyte.[11]

Integration of the surface-confined peak gives a charge of 1.8 × 10^{11} C, corresponding to a density of $Fe(CN)_6^{4-}$ anions of 1.4 × 10^{14} molecules cm^{-2}. This number is equivalent to approximately 4 monolayers of $Fe(CN)_6^{3-}$ (3.4 × 10^{13} molecules cm^{-2}).[36] COMSOL fits to the anodic linear sweep of the CV with 9 m LiTFSI with 5 mM $Fe(CN)_6^{3-}$ in the absence of Zn^{2+} yielded a $D_O = 1 \times 10^{-6}$ and a $k^0 = 0.005$ cm s^{-1}, similar to that reported previously.[11]

As the $Zn(TFSI)_2$ concentration is increased from 0 to 1.75 mM, represented in the CVs toward the bottom of Figure 1A, the magnitude of the peak between 0.0 and 0.05 V associated with confined $Fe(CN)_6^{3-}$ decreases. This decrease is likely not associated with interference from Zn electrodeposition because the potential range used here is ca. 0.89 V positive of the Zn^{2+} reduction potential. The concentration of $Zn(TFSI)_2$ was systematically increased until the resultant CV exhibited the sigmoidal shape expected in the absence of confinement. This ultimate concentration is 1.75 mM. Accompanying this change is a drop in the density of confined $Fe(CN)_6^{4-}$ to 5.4 × 10^{13} at 1.25 mM $Zn(TFSI)_2$, then to below one monolayer of coverage at 6.7 × 10^{12} molecules cm^{-2} at 1.50 mM $Zn(TFSI)_2$. COMSOL fits to the anodic linear sweep again yielded D_O values ranging from 1 × 10^{-6} to 8 × 10^{-7} cm^2 s^{-1} and a k^0 = 0.005 cm s^{-1} (absent Zn^{2+} addition) to k^0 = 0.002 cm s^{-1} with the addition of 1.75 mM Zn^{2+}. The lower value of k^0 suggests that Zn^{2+} addition has inhibited $Fe(CN)_6^{3-/4-}$ electron transfer at the interface.

To evaluate the effect of the addition of other multivalent cations on the $Fe(CN)_6^{4-}$ confinement structure, we examined the effect of Ca^{2+}, Mg^{2+}, and Al^{3+} additions on the

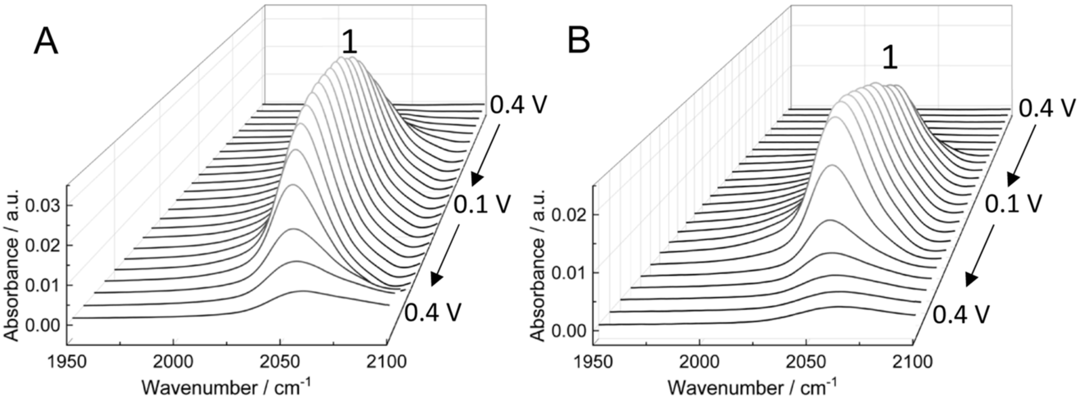

Figure 2. Potential-dependent SEIRAS spectra in the 1950−2100 cm^{-1} region showing ν(CN) peaks from $[Fe(CN)_6]^{4-}$ and $[Fe(CN)_6]^{3-}$ (A) 9 m LiTFSI + 1.75 mM $Zn(TFSI)_2$ + 20 mM $K_3Fe(CN)_6$, and (B) 9 m LiTFSI + 20 mM $K_3Fe(CN)_6$.

voltammetry. Figure 1B reports CVs obtained from a Pt UME in 5 mM $K_3Fe(CN)_6$ and 9 m LiTFSI as a function of added $Ca(TFSI)_2$. As before, the CV obtained prior to $Ca(TFSI)_2$ addition exhibits the confinement peak also reported in Figure 1A. Integration of this peak at 0 mM $Ca(TFSI)_2$ yielded a density of $Fe(CN)_6{}^{4-}$ ions of 6 × 10^{14}. In contrast to the Zn^{2+} case, however, the addition of $Ca(TFSI)_2$ does not result in a decrease in the confinement peak. Rather, at the first addition of 50 mM $Ca(TFSI)_2$ a doubling of $Fe(CN)_6{}^{4-}$ ion density to 1.2 × 10^{15} molecules cm^{-2} was observed. The addition of a greater concentration of $Ca(TFSI)_2$ than $Zn(TFSI)_2$ was necessary to obtain an observable increase in the confinement peak intensity. As $Ca(TFSI)_2$ concentration is increased past 50 mM $Fe(CN)_6{}^{4-}$ ion density at the interphase continues to increase less rapidly, reaching a maximum of 1.64 × 10^{15} at a Ca^{2+} concentration of 150 mM before declining to 1.59 × 10^{15} molecules cm^{-2} at the final Ca^{2+} concentration of 200 mM. This increase is accompanied by an increase in the potential of the oxidation peak relative to E_O from 0.035 to 0.061 V from 0 to 50 mM Ca^{2+}, an increase of 0.026 V that persists with further increase in $Ca(TFSI)_2$ concentration. COMSOL fits show that D_O decreases monotonically from 9 × 10^{-7} to 5 × 10^{-7} cm^2 s^{-1} as $Ca(TFSI)_2$ concentration is increased from 0 mM to 200 mM, possibly a consequence of the increased $Fe(CN)_6{}^{4-}$ confined at the interphase. Also determined through COMSOL simulations, k^0 remained = 0.004 cm s^{-1} for all Ca^{2+} concentrations.

CVs obtained from a Pt UME in 5 mM $K_3Fe(CN)_6$ and 9 m LiTFSI as a function of added $Mg(TFSI)_2$ are represented in Figure 1C. As $Mg(TFSI)_2$ concentration is increased in Figure 1C, the confinement peak is maintained and increases its size, similar to the case of $Ca(TFSI)_2$ addition in Figure 1B. Smaller 10 mM increments of $Mg(TFSI)_2$ concentration increase were used, and the maximum concentration of $Mg(TFSI)_2$ employed was 50 mM, both values less than those used for $Ca(TFSI)_2$, in order to obviate solution viscosity issues, which produced voltametric anomalies at higher concentrations of $Mg(TFSI)_2$. The first addition of 10 mM $Mg(TFSI)_2$ is accompanied by an increase in interfacial $Fe(CN)_6{}^{4-}$ ion density from 4.9 × 10^{14} to 6.7 × 10^{14} molecules cm^{-2}. The increase in interfacial $Fe(CN)_6{}^{4-}$ ion density with Mg^{2+} concentration continues until reaching a maximum of 8.36 × 10^{14} molecules cm^{-2} at the highest Mg^{2+} concentration of 50 mM. We also observed an increase in the oxidation peak position relative to E_O in Figure 1C of 0.02 V upon the first addition of 10 mM $Mg(TFSI)_2$. Additionally, as determined by COMSOL fits, D_O decreases somewhat from 9 × 10^{-7} cm^2 s^{-1} at 0 mM $Mg(TFSI)_2$ to 6 × 10^{-7} cm^2 s^{-1} at 50 mM $Mg(TFSI)_2$. This decrease in D_O is again likely associated with the increased amount of $Fe(CN)_6{}^{4-}$ confined in the interphase. Also determined through COMSOL simulations, k^0 = 0.004 cm s^{-1} at all $Mg(TFSI)_2$ concentrations.

Figure 1D shows CVs obtained from a Pt UME in 5 mM $K_3Fe(CN)_6$ and 9 m LiTFSI as a function of added $Al(TFSI)_3$. Absent Al^{3+} addition, there is a confinement peak present between 0.00 and 0.05 V on the anodic scan. Integration of this peak results in an initial density of $Fe(CN)_6{}^{4-}$ ions of 1.69 × 10^{14} molecules cm^{-2}. The addition of $Al(TFSI)_3$ results in a decrease in the magnitude of the confinement peak in Figure 1D, a trend that continues until the peak is no longer observable at a concentration of 1.25 mM. This behavior is similar to that observed with Zn^{2+} addition and opposite to that observed with Ca^{2+} and Mg^{2+} addition, but the concentration of $Al(TFSI)_3$ needed to eliminate an observable confinement peak is 0.5 mM lower than that for $Zn(TFSI)_2$. Finally, COMSOL fits to the anodic linear sweep of the CVs determined that D_O decreases from a value of 9 × 10^{-7} cm^2 s^{-1} absent Al^{3+} to a value of 4 × 10^{-7} cm^2 s^{-1} at 1.25 mM while k^0 = 0.004 cm s^{-1} (absent Al^{3+} addition) moves to k^0 = 0.001 cm s^{-1} with the addition of 1.25 mM Al^{3+}. Similar to the Zn^{2+} case, the lower value of k^0 suggests that Al^{3+} addition has also inhibited $Fe(CN)_6{}^{3-/4-}$ electron transfer at the interface.

3.2. SEIRAS of Ferro(i)cyanide Redox within Water-In-Salt Electrolytes.

To further evaluate the effect of Zn^{2+} addition on the persistence of $[Fe(CN)_6]^{4-}$ at the solid−liquid interphase, we performed potential-dependent SEIRAS measurements on a Au surface immersed in an electrolyte containing 9 m LiTFSI + 20 mM $K_3Fe(CN)_6$ with no additional $Zn(TFSI)_2$ and 1.75 mM $Zn(TFSI)_2$. The region of the SEIRAS spectra between 1950 and 2100 cm^{-1} is shown in Figure 2, which contains the peak attributed to the ν(CN) stretch of $[Fe(CN)_6]^{4-}$ (peak 1).[37] There is little change shown in the spectrum over the baseline (obtained at 0.4 V) until a potential of 0.35 V is reached, where peak 1 associated with $[Fe(CN)_6]^{4-}$ appears in both cases. Peak 1 persists as the potential scan is reversed until finally decreasing to the baseline.

Figure 3 reports the normalized intensities of peak 1 in 9 m LiTFSI without (black) and with 1.75 mM $Zn(TFSI)_2$ present (red). As potential is initially swept negative, the potential is then swept to positive values; the intensity of peak 1 achieves a maximum and then decreases. Interestingly, in the presence of

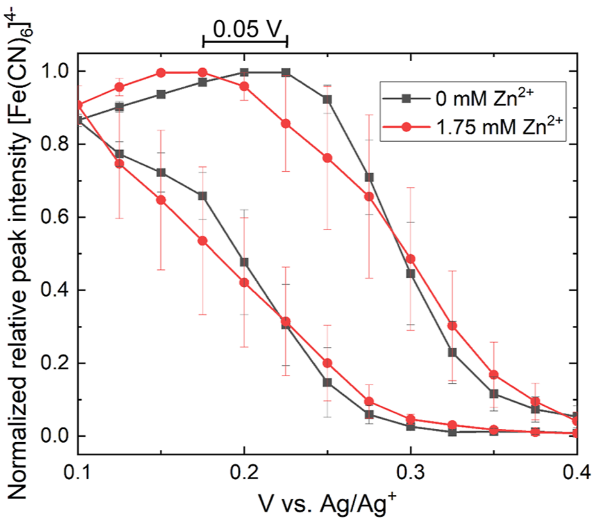

Figure 3. Normalized peak intensities of ν(CN) $[Fe(CN)_6]^{4-}$ (peak 1) via SEIRAS. Nine m LiTFSI + 20 mM $K_3Fe(CN)_6$ (black square) and 9 m LiTFSI + 1.75 mM $Zn(TFSI)_2$ + 20 mM $K_3Fe(CN)_6$ (red circle).

Zn^{2+}, this maximum occurs some 0.05 V more negative than in the absence of this cation. The delayed decrease in peak 1 intensity in the absence of Zn^{2+} is evidence that there is $[Fe(CN)_6]^{4-}$ at the interphase that is not immediately oxidized upon the anodic sweep. Alternatively, in the presence of Zn^{2+}, interfacial $[Fe(CN)_6]^{4-}$ is oxidized more readily.

3.3. SEIRAS of Water-In-Salt Electrolyte Species.

3.3.1. Surface Spectroscopy of 20 m LiTFSI WiSE with and without 1 m Zn(TFSI)$_2$. Figure 4A,B reports SEIRA spectra obtained at 0.61 V vs Ag/Ag^+ subtracted from a baseline obtained at −0.69 V vs Ag/Ag^+. Figure 4A is from 20 m LiTFSI + 1 m $Zn(TFSI)_2$ in water, while Figure 4B is from 20 m LiTFSI absent $Zn(TFSI)_2$ addition. The $TFSI^-$ anion exhibits 39 normal modes, with the highest 11 in energy between 1000 and 1400 cm^{-1}.[38] Of these 11, 8 are typically seen in the IR.[38] In Figure 4, 7 of these modes are labeled a-g, and the eighth, a weak $\nu_{as}(CF_3)$ mode at 1225 cm^{-1}, is not observed. Assignments for these modes are reported in Table 1, along with previously calculated vibrational frequencies for $TFSI^-$.[38]

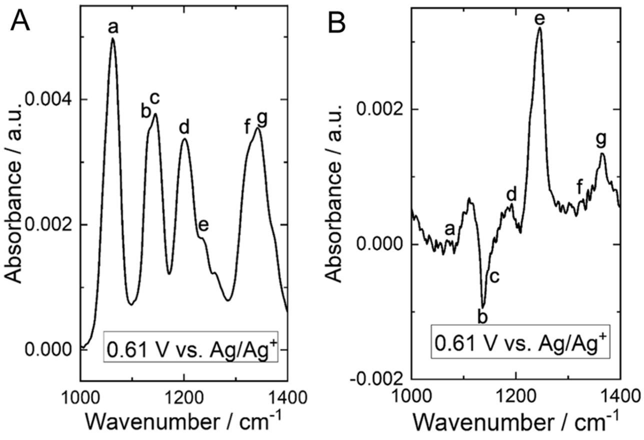

Figure 4. SEIRA spectra of (A) 20 m LiTFSI + 1 m $Zn(TFSI)_2$ and (B) 20 m LiTFSI. Spectra shown were taken at 0.61 V and subtracted from a baseline at −0.69 V. Letters correspond to peak assignments in Table 1.

Table 1. Peak Assignments for SEIRA Spectrum at 0.61 V vs. Ag/Ag^+ Subtracted from a Baseline at −0.69 V vs. Ag/Ag^+ of 20 m LiTFSI + 1 m $Zn(TFSI)_2$

peak	assignment	energy/cm^{-1} (LiTFSI only)	energy/cm^{-1} (1 m Zn^{2+})	calculated energy/cm^{-1}[38]
a	$\nu_{as}(SNS)$	1058	1060	1056
b	$\nu_s^{IP}(SO_2)$	1130	1134	1133
c	$\nu_s^{OOP}(SO_2)$	1145	1145	1139
d	$\nu_{as}(CF_3)$	1199	1199	1198
e	$\nu_s(CF_3)$	1245	1245	1237
f	$\nu_{as}^{OOP}(SO_2)$	1330	1330	1330
g	$\nu_{as}^{IP}(SO_2)$	1365	1359	1354

When $Zn(TFSI)_2$ is present, as shown in Figure 4A, all peaks associated with $TFSI^-$ increase at 0.61 V relative to that at −0.69 V. This increase suggests that the concentration of $TFSI^-$ at the interphase becomes greater at positive potentials in this solution. In Figure 4B, absent $Zn(TFSI)_2$ addition, peaks at −0.69 V are present as both positive and negative-going features, and some peaks are absent. In particular, peak a associated with $\nu_{as}(SNS)$ has not changed relative to the baseline, while peak e associated with $\nu_s(CF_3)$ increases. Peaks b and c associated with the asymmetric SO_2 stretch decrease relative to the baseline. The presence of intensity associated with the symmetric CF_3 stretch of $TFSI^-$ at positive potential is consistent with prior work and suggests that the concentration of $TFSI^-$ at the interphase increases at positive potentials.[11] Alternatively, the differences in intensity of peaks a-d and f relative peak e suggest that the molecule may have reoriented relative to its position at −0.69 V (vide infra).

3.3.2. Potential Dependence of Surface Spectroscopy Peaks in 20 m LiTFSI with and without 1 m Zn(TFSI)$_2$. To investigate how the presence of Zn^{2+} influences potential-dependent speciation at the interphase, we performed in situ SEIRAS on the LiTFSI WiSE and the LiTFSI + $Zn(TFSI)_2$ WiSE. Figure 5A reports difference spectra obtained from a solution containing 20 m LiTFSI. Peaks e and g are assigned above, along with the water bending mode[39] at 1611 cm^{-1} (peak h). In the absence of Zn^{2+}, modes associated with $TFSI^-$ increase at positive potentials, while the water bending mode (peak h) appears as a negative-going feature.

Figure 5C reports the normalized potential dependence of the intensities of bands e, g, and h from the spectra in Figure 5A. As potential is increased from −0.69 to 0.61 V peaks, e and g[18,26,38,40,41] increase in intensity. This increase indicates a greater surface excess of the anion at more positive potentials relative to −0.69 V. Simultaneously, peak h, assigned to the bending mode of water $\delta(H_2O)$, decreases in intensity, indicating a decrease in surface excess of water at more positive potentials relative to −0.69 V. This behavior is consistent with prior results,[11] which concluded that $TFSI^-$ is enriched at positive potentials, while water modes associated with Li^+ coordination were enriched at negative potentials. The present data feature the water bending mode as opposed to the OH stretch used previously.

We note that the water bending mode, $\delta(H_2O)$, is found at 1611 cm^{-1} in this electrolyte. This value is somewhat lower energy relative to $\delta(H_2O)$, which is ~1650 cm^{-1} in pure liquid water and is instead closer to $\delta(H_2O)$ = ~1590 cm^{-1} of water

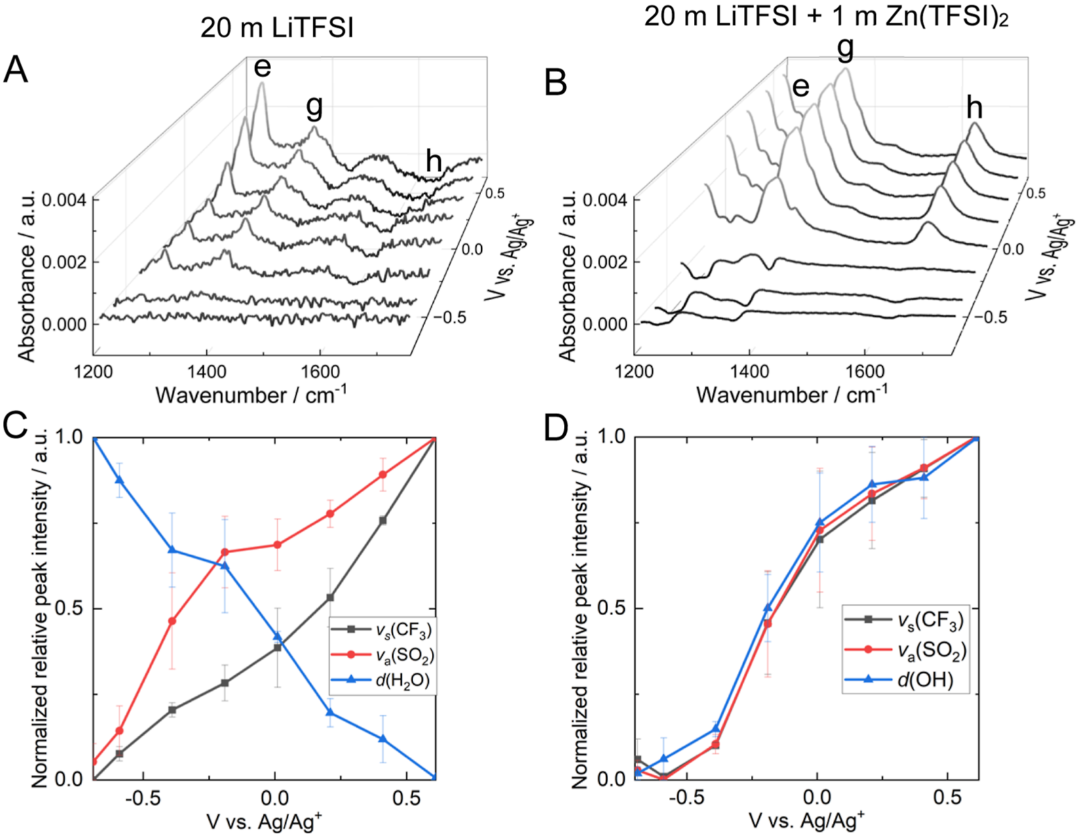

Figure 5. SEIRAS spectra of (A) 20 m LiTFSI WiSE and (B) 20 m LiTFSI + 1 m Zn$(TFSI)_2$ WiSE, and normalized peak intensities for selected bands of (C) 20 m LiTFSI WiSE and (D) 20 m LiTFSI + 1 m Zn$(TFSI)_2$ WiSE.

in the gas phase.[39] The origin of this shift is likely due to a change in the degree of H-bonding in the more concentrated electrolyte, as has been discussed previously.[11,42] We also note that there are no TFSI$^-$ peaks above 1450 cm^{-1} that could contribute to spectral congestion in this region.[18,26,38,40,41]

Figure 5B reports the spectra obtained from a solution containing 20 m LiTFSI + 1 m Zn$(TFSI)_2$ under the same conditions as in Figure 5A. Peaks e, g, and h are present in the spectra, as shown in Figure 5A. Figure 5D reports the normalized potential dependence of these bands. In Figure 5B, the energy of peak h, $\delta(H_2O)$, is 1635 cm^{-1}, which is closer to that found in pure water at 1650 cm^{-1} than the $\delta(H_2O)$ peak in Figure 5A obtained without Zn$(TFSI)_2$ addition. The blue shift of $\delta(H_2O)$ in the presence of Zn^{2+} suggests that H-bonding at the interphase is restored relative to that in the Li-alone case.

Figure 5B,D shows that as the potential is increased from −0.69 to 0.61 V, peaks e and g increase in intensity relative to the baseline at −0.69 V, indicating an increase in surface excess of the TFSI$^-$ anion as potential increases. Interestingly, the intensity of peak h also increases as the potential is made more positive, a result that is also found with the OH stretch at higher energy (Figure S2). This increase in peak h suggests that the surface excess of water follows that of TFSI$^-$ in the presence of Zn^{2+}, a result opposite that found in the absence of Zn^{2+}.

3.3.3. SEIRAS of WiSE with Additional Multivalent Cations. To evaluate whether trends of TFSI$^-$ and water speciation at the interphase occur in the presence of other cations, we performed potential-dependent spectroscopy of the WiSE with the addition of 1 m Ca$(TFSI)_2$, 0.5 m Mg$(TFSI)_2$, and 0.1 m Al$(TFSI)_3$. The concentrations of Mg$(TFSI)_2$ and Al$(TFSI)_3$ are reduced compared to the other salts due to their lower solubility. For Al$(TFSI)_3$-containing WiSE, the LiTFSI concentration is also reduced to 15 m due to the low solubility of Al$(TFSI)_3$.

Figure 6A reports the surface-enhanced infrared spectra of 20 m LiTFSI WiSE with the addition of 1 m Ca$(TFSI)_2$. The trends for peak intensity are consistent with the 20 m LiTFSI case. As the potential is swept positively, peaks from the TFSI$^-$ anion (e and g) increase in intensity, indicating an increase in surface excess with potential for those species. At the same time, peak h, which is assigned to the water OH bend decreases in intensity, indicating a decrease in surface excess of water, presumably as water is displaced from the interphase by anion. This decrease indicates that a water-rich layer is displaced by a TFSI$^-$-rich layer as the potential is swept positive.

Figure 6B reports the potential dependence of the normalized intensities of bands of peaks e, g, and h. Peaks e and g (associated with TFSI$^-$) increase in intensity with potential, while the intensity of peak h ($\delta(H_2O)$) decreases with potential. These peak intensity trends are the same as seen in Figure 5A for LiTFSI WiSE, so the 20 m LiTFSI + 1 m Ca$(TFSI)_2$ WiSE trends are classified as Li-like.

Figure 6C shows the surface-enhanced infrared spectra of a 20 m LiTFSI WiSE with the addition of 0.5 m Mg$(TFSI)_2$ under the same conditions as Figure 6A. TFSI$^-$ peaks e and g and the water OH bend peak h are present in Figure 6C. Like in Figure 6A, peaks e and g are positive-going at more positive potentials, and peak h is negative-going at more positive potentials. Likewise, the potential-dependent intensity trends

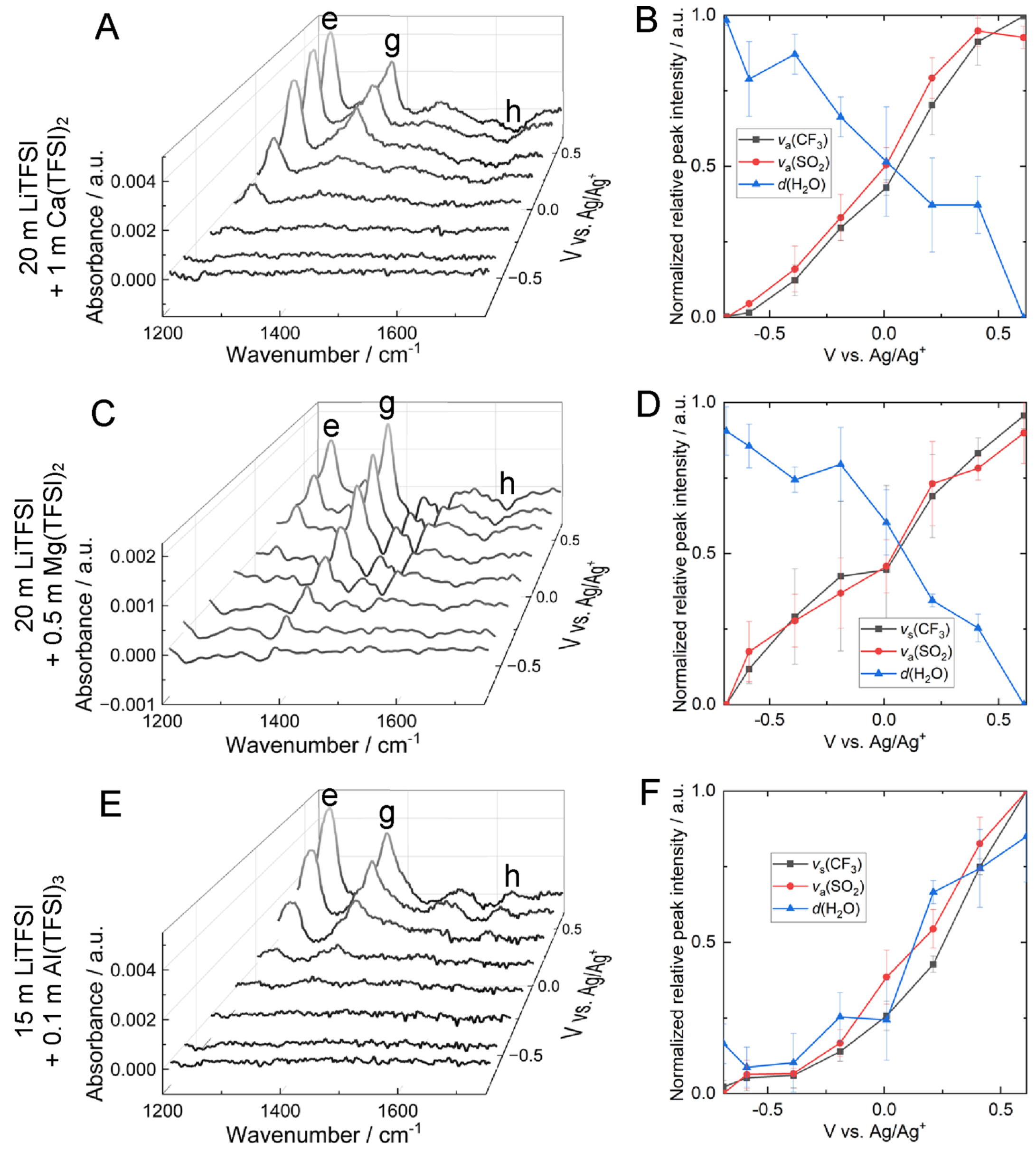

Figure 6. Potential-dependent SEIRAS LiTFSI WiSE with additional multivalent cations and selected peak intensities. (A) Spectra obtained from 20 m LiTFSI WiSE + 1 m Ca(TFSI)$_2$ WiSE and (B) normalized peak intensities for selected bands. (C) Spectra obtained from 20 m LiTFSI WiSE + 0.5 m Mg(TFSI)$_2$ WiSE and (D) normalized peak intensities for selected bands. (E) Spectra obtained from 15 m LiTFSI + 0.1 m Al(TFSI)$_3$ WiSE and (F) normalized peak intensities for selected bands.

of peaks e, g, and h in Figure 6D for the Mg(TFSI)$_2$-containing WiSE can also be classified as Li-like.

Figure 6E reports the SEIRA spectra of a 15 m LiTFSI WiSE + 0.1 m Al(TFSI)$_3$. The two most intense peaks from the TFSI$^-$ anion (peaks e and g) as well as the water bending mode (peak h) are seen in the spectra at positive potentials. Figure 6F shows the normalized potential dependence of the intensities of bands of peaks e, g, and h. Similar to the case with Zn^{2+} addition, the addition of Al(TFSI)$_3$ to the WiSE results in all three peaks increasing in intensity with the potential. We classify these trends as Zn-like.

3.4. Interfacial Layering Structure Probed by AFM. To investigate the effect of multivalent cations on interfacial layering nanostructures, we performed potential-dependent force spectroscopy measurements by using AFM. Under all conditions, the measured force−distance curves reveal steps or discontinuities in the force profile; Figures S4 and S5 show representative results. The steps reflect the arrangement of ions and water in layers at the smooth electrolyte/electrode interface: as a layer of ions and/or water molecules is ruptured or pushed through with the sharp tip, a step appears in the force profile.[11,27] A higher force typically suggests a stronger adsorption of the molecules or ions, either to the surface or to the underlying layer. The solvation structure vanishes beyond ∼3 layers at all conditions. Roughness can disturb interfacial layering in aqueous solutions, but the small surface roughness (<2 Å) in the regions selected for the AFM measurements (50 nm × 50 nm) facilitates the detection of these layers.

Heat maps of the force−distance curves in 21 m LiTFSI WiSE reported in our earlier work[11] showed excellent agreement between force−distance curves at different locations. With the addition of multivalent cations, the steps

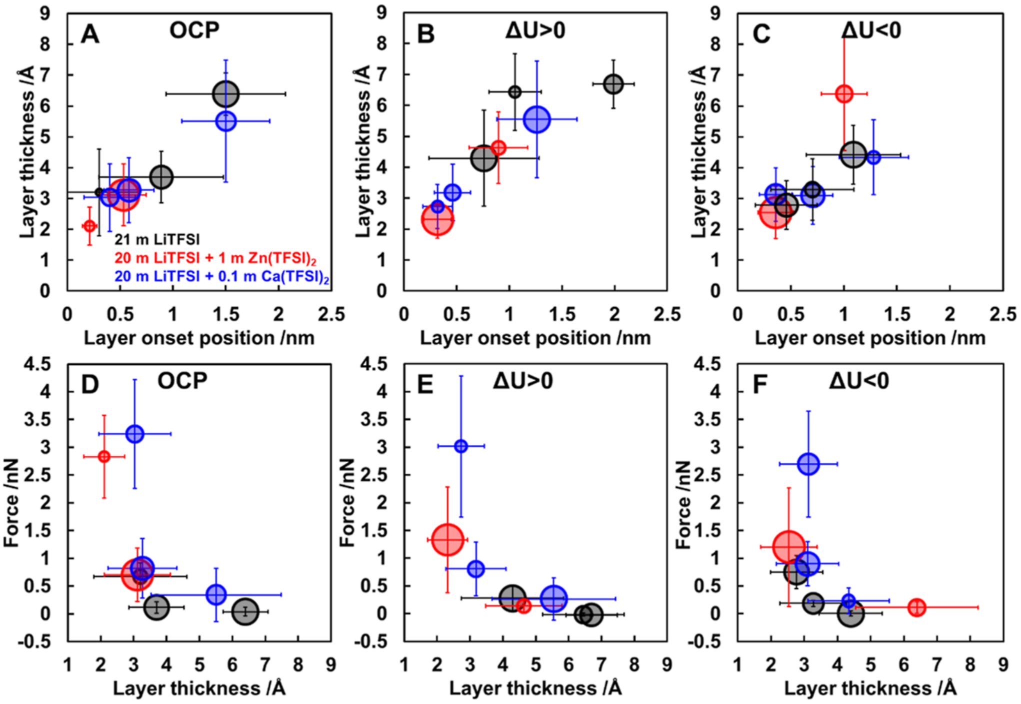

Figure 7. Bubble diagrams with the layer thickness vs the onset position of the layer and rupture force vs layer thickness at (A,D) OCP, (B,E) $\Delta U > 0$, (C,F) $\Delta U < 0$ for 21 m LiTFSI (black), 20 m LiTFSI + 1 m $Zn(TFSI)_2$ (red), and 20 m LiTFSI + 0.1 m $Ca(TFSI)_2$ (blue). Each bubble represents a cluster of data points in the scatter plot. Bubble position and error bars are the average and standard deviation of each group of layers, respectively. Bubble size is proportional to the frequency of measurement of each layer. OCP for 21 m LiTFSI is −0.16 V vs Ag, for 20 m LiTFSI + 1 m $Zn(TFSI)_2$ is 1.0 V vs Zn/Zn^{2+}, and for 20 m LiTFSI + 0.1 m $Ca(TFSI)_2$ is 0.13 V vs Ag. The positive potentials with respect to OCP ($\Delta U = U - U_{OCP} > 0$) for 21 m LiTFSI, 20 m LiTFSI + 1 m $Zn(TFSI)_2$, and 20 m LiTFSI + 0.1 m $Ca(TFSI)_2$ shown in (B,E) are $\Delta U = +0.46$ V (0.3 V vs Ag), $\Delta U = +0.4$ V (1.4 V vs Zn/Zn^{2+}), and $\Delta U = +0.27$ V (0.4 V vs Ag), respectively. The negative potentials with respect to OCP ($\Delta U = U - U_{OCP} < 0$) in (C,F) are $\Delta U = -0.24$ V (−0.4 V vs Ag), $\Delta U = -0.4$ V (0.6 V vs Zn/Zn^{2+}), and $\Delta U = -0.23$ V (−0.1 V vs Ag), respectively.

can still be clearly resolved on individual force−distance curves, but when superposed in a heat map, the steps cannot be distinguished. This variability reveals that the interfacial structure changes slightly with location, possibly due to the heterogeneous distribution of the divalent ions on the gold surface (Figures S4 and S5). Hence, we analyzed each force curve separately to determine the thickness, onset position, and rupture force of each layer, and 2−3 groups of layers were identified from scatter plots for each force map. The layer thickness vs layer onset position and the rupture force vs layer thickness are shown in bubble diagrams in Figure 7.

Figure 7 shows that, overall, the layered interface is thicker in 21 m LiTFSI and 20 m LiTFSI + 0.1 m $Ca(TFSI)_2$, as inferred from the greater onset position (up to ∼1.5 nm) and more layers present at the surface, relative to 20 m LiTFSI + 1 m $Zn(TFSI)_2$ WiSE. In highly concentrated electrolytes like WiSE, the diffuse layer collapses (Debye length <0.1 nm), and hence, these layers inform about the layered structure of (polyatomic) ions (and water) that arrange on the surface to counterbalance the surface potential. Hence, the layer thickness depends on the molecular composition. Note that in highly concentrated electrolytes, overscreening by counterions is expected,[43] and hence, multiple layers of counter- and co-ions accumulate at the interface to counterbalance the surface charge, deviating from the concept of the Stern layer in dilute electrolytes.[44] Additional factors can influence the layer thickness, such as the ion packing disorder, the compressibility of the molecules and hydrated ions (at applied pressures as high as 0.5 GPa with the tip), and the potential dehydration of ions induced by pressure.[45,46] Indeed, previous molecular dynamics (MD) simulations for ionic liquids proposed that the compressibility of ions under high pressures can lead to a significant reduction in layer thickness. Therefore, the layer thickness might appear smaller than the inherent molecular/ion size.

3.4.1. Interfacial Layering Structure Probed by AFM at Negative Bias.

The interfacial structure probed by AFM changes as a function of the potential. We expect that Li^+, Ca^{2+}, and Zn^{2+} interact strongly with negatively biased surfaces, and hence, we describe these results first. For 21 m LiTFSI, three layers are measured with $\Delta_3 = 4.3 \pm 1.0$, $\Delta_2 = 3.3 \pm 1.0$, and $\Delta_1 = 2.8 \pm 0.8$ Å as the force increases, i.e., as the layer onset position decreases. The ca. 3 ± 1 Å layers are likely attributed to water or hydrated Li^+ at the interface, considering the negative applied potential and the relatively compact layer thickness. These findings are consistent with the SEIRAS results. The observed reduction in layer thickness compared to the calculated size of $[Li(H_2O)]^{4+}$ reported (ca. 5.4 Å)[11] is likely a consequence of the dehydration of the Li^+ upon its adsorption to the surface. For example, Lee et al.[46] investigated LiCl solutions and found a distinct Li^+ layer at 2.2−2.4 Å from the mica surface, followed by a less pronounced layer located at 5 Å further away from the surface, which was associated with partially dehydrated and highly hydrated Li^+, respectively. Therefore, it is possible that layer $\Delta_2 = 3.3 \pm 1.0$ Å is associated with the partial dehydration of the adsorbed $[Li(H_2O)_x]^+$, and the layer resolved at much higher force ($\Delta_1 = 2.8 \pm 0.8$ Å) is attributed to surface-adsorbed Li^+; a dehydration-associated step has been previously reported in SFA experiments for dilute electrolytes.[47] An additional factor contributing to the smaller dimension could be the compression exerted by the tip. For example, previous studies have reported a distortion of the solvation shell induced by the AFM tip pressure, coupled with the adsorption to the electrode surface for Li^+ ions chelated to oligoether ligands with 3 to 4 repeating units.[48,49]

There are multiple possible explanations for the layer with a thickness of $\Delta_3 \sim 4.3$ Å. First, we note the 4.3 ± 1.0 Å layer thickness is close to the predicted size for hydrated Li^+, which might suggest the existence of a second layer rich in $[Li(H_2O)_x]^+$ to further counterbalance the surface potential. The presence of two solvation layers enriched in hydrated Li^+ could indicate a phenomenon known as crowding of multiple layers of counterions in highly concentrated electrolytes, particularly at sufficiently high potentials.[43] On the other hand, overscreening is possible, and hence, $TFSI^-$ may also be present close to the negative Au surface. Previous studies of $TFSI^-$ containing ionic liquids have found a $TFSI^-$-rich layer of ca. 4.4 Å, which is very close to the 4.3 ± 1.0 Å spacing measured here and slightly smaller than the values calculated based on the packing dimension (4.7 Å) and the van der Waals diameter (5.3 Å).[49−51] We note the 4.3 ± 1.0 Å spacing is also observed at $\Delta U > 0$, where the interface is anticipated to be rich in $TFSI^-$.

In the electrolyte with Ca^{2+} at negative bias ($\Delta U < 0$), three groups of layers ($\Delta_1 = 3.1 \pm 0.9$, $\Delta_2 = 3.1 \pm 0.9$, and $\Delta_3 = 4.3 \pm 1.2$ Å) are measured, and hence, they are similar to the results for 21 m LiTFSI WiSE. This similarity and the larger radius of the first hydration shell of Ca^{2+} compared to Li^+ (4.12 vs 3.82 Å)[52] suggest that the interfacial region may be populated with $[Li(H_2O)_x]^+$ and $[Ca(H_2O)_x]^{2+}$; the differences among force−distance curves taken at different positions are consistent with Ca^{2+} and Li^+ being both present at different locations. In contrast, only two layers ($\Delta_1 = 2.5 \pm 0.9$ and $\Delta_2 = 6.4 \pm 1.8$ Å) are observed in 20 m LiTFSI + 1 m $Zn(TFSI)_2$ WiSE. The layer close to the surface is presumably rich in water and Zn^{2+}. The size of Δ_2 is too large to be associated with a single cation or anion. The large standard deviation of Δ_2 suggests the presence of multiple species of different sizes, presumably strongly hydrated $[Zn(H_2O)_x]^{2+}$, as well as clusters of cations with $TFSI^-$. These large clusters were not detected in the other two electrolytes.

3.4.2. Interfacial Layering Structure Probed by AFM at Positive Bias.

In 21 m LiTFSI WiSE at $\Delta U > 0$, a different interfacial structure is observed: $\Delta_1 = 4.3 \pm 1.6$, $\Delta_2 = 6.4 \pm 1.2$, and $\Delta_3 = 6.7 \pm 0.8$ Å. Here, layers rich in water are repelled from the Au electrode and replaced by layers abundant in $TFSI^-$, as inferred from the SEIRAS results. The layer thickness $\Delta_1 = 4.3 \pm 1.6$ Å is attributed to $TFSI^-$, as previously discussed. However, we cannot completely rule out the occasional presence of the cation given that layers of approximately 3 Å thickness are sometimes detected, as inferred from the large error bars of Δ_1. Layers with thickness 6.4 ± 1.2 and 6.7 ± 0.8 Å are observed at $\Delta U > 0$ but not at $\Delta U < 0$. Hence, these larger solvation layers are likely associated with $[Li(H_2O)_x]^+([TFSI]^-)_y$ clusters, as proposed previously.[11] Overall, solvation layers resolved farther from the surface could have a higher number of co-ions and be more loosely packed and less strongly bound to the surface compared to the surface-adsorbed layers.

In the 20 m LiTFSI WiSE with 0.1 m Ca^{2+} at $\Delta U > 0$, the interfacial structure also features 3 layers with thickness $\Delta_1 = 2.7 \pm 0.7$, $\Delta_2 = 3.2 \pm 0.9$, and $\Delta_3 = 5.5 \pm 1.9$ Å, with a larger portion of the larger layers. The interfacial layering differs from the results obtained in the absence of divalent cations, which indicates that Ca^{2+}, despite its small concentration, disturbs the electrical double layer. This is interesting because there was no significant difference at $\Delta U < 0$. Although the size of the first layer is only ∼2.7 Å, the force required to push through this layer is very large (∼3 nN), which indicates it is very strongly adsorbed. This, along with the surface enrichment of $TFSI^-$ and depletion of water inferred from SEIRAS, suggests that this layer must indeed be rich in $TFSI^-$, strongly bound to the surface and compressed by the tip. This could also apply to the second layer. Note that the thickness of the third layer and the onset separation are widely distributed (Δ_3 from 7.5 to 3.8 Å and D_2 from 0.9 to 1.7 nm) compared to the absence of divalent cations. Hence, it is likely that Ca^{2+} is coordinated with $TFSI^-$ and forms clusters that approach the surface, so that a mixture of $TFSI^-$, $[Ca(H_2O)_x]^{2+}([TFSI]^-)_y$, and possibly $[Li(H_2O)_x]^+([TFSI]^-)_y$ clusters are present here. Higher concentrations of Ca^{2+}, like those used in SEIRAS experiments, are hypothesized to enhance the amount of Ca^{2+}-clusters in the bulk and, therefore, their presence at the interface.

Theory has shown for other highly concentrated electrolytes (ionic liquids) that the cluster-like structure in the electrolyte can be modified in the proximity of a charged surface, deviating from the bulk structure, where the electric field is zero.[53,54] This could explain why, e.g., Ca^{2+} disrupts the EDL of the WiSE more significantly at positive than at negative potentials, while the bulk structure remains the same.

In the presence of Zn^{2+}, only two layers of thickness, $\Delta_1 = 2.3 \pm 0.6$ (most frequent) and $\Delta_2 = 4.6 \pm 1.2$ Å (less frequent), are measured at positive bias ($\Delta U > 0$), indicating the disruption of the WiSE EDL by Zn^{2+}. The smaller size of the layers is consistent with the increase in water content detected by SEIRAS, compared to the negative potential (baseline), and hence, it is attributed to the presence of water, along with an anion-rich interface; indeed, Δ_2 is close to the size attributed to $TFSI^-$.

3.4.3. Interfacial Layering Structure Probed by AFM at OCP.

In 21 m LiTFSI WiSE, three distinct layers are measured within a separation of 1.5 nm from the surface: $\Delta_1 = 3.2 \pm 1.4$, $\Delta_2 = 3.7 \pm 0.8$, and $\Delta_2 = 6.7 \pm 0.7$ Å, respectively. The layer thickness reflects an intermediate situation between the positive and negative potentials discussed above, suggesting the coexistence of both $[Li(H_2O)_x]^+$ and $[Li(H_2O)_x]^+([TFSI]^-)_y$ near the surface, maintaining electroneutrality. The structure in 20 m LiTFSI + 0.1 m $Ca(TFSI)_2$ is similar to 21 m LiTFSI at OCP ($\Delta_1 = 3.0 \pm 1.1$, $\Delta_2 = 3.3 \pm 1.0$, and $\Delta_3 = 5.5 \pm 2.0$ Å), but the standard deviation is greater, reflecting the greater heterogeneity of the interface, as described earlier. Based on the observations at positive and negative bias, these results indicate the presence of $[Li(H_2O)_x]^+$, $[Li(H_2O)_x]^+([TFSI]^-)_y$, $[Ca(H_2O)_x]^{2+}([TFSI]^-)_y$, and water molecules near the surface. In the case of Zn^{2+}, layers are only detected at ∼0.5 nm from the surface, with a small thickness (2−3 Å), consistent with the presence of water, the absence of clusters, and/or the reduction of overscreening near the Au surface at OCP. This indicates that the addition of Zn^{2+} not only disrupts the WiSE structure near a positive and negative Au surface but also even in the absence of an applied bias. Note that the surface charge of unbiased gold in aqueous solution has been reported to be both slightly positive[55] and negative,[56] and; hence, we cannot exclude a small surface charge for the unbiased Au.

4. DISCUSSION

4.1. Ultramicroelectrode Experiments. The measurements reported above show that the addition of foreign metal cations to the WiSE has different effects depending on cation identity. Cyclic voltammetry measurements probing $Fe(CN)_6^{3-/4-}$ redox at a UME in a concentrated LiTFSI solution all feature a peak indicative of interphase-confined $Fe(CN)_6^{4-}$, as reported previously.[11] In the presence of Zn^{2+} and Al^{3+}, the same UME measurements show that this confined peak decreases with increasing cation addition. Alternatively, the same measurements performed in the presence of Ca^{2+} or Mg^{2+} show retention and even enhancement of the $Fe(CN)_6^{4-}$ confinement peak.

We previously suggested that the confinement peak seen in WiSE was a consequence of the layering of the electrolyte at the interphase. Specifically, at the $Fe(CN)_6^{3-/4-}$ redox potential (>0 V vs Ag/Ag^+), we suggested a $TFSI^-$-rich layered, double-layer structure is present at the interphase. The layered structure combined with the hydrophobicity of the $TFSI^-$-rich layer inhibits diffusion of the hydrophilic $Fe(CN)_6^{4-}$ molecule away from the electrode surface as it is generated, resulting in a high local concentration of the reduced species at the interphase.[11] Further, because the size of the confinement peak is tied to the density of $Fe(CN)_6^{4-}$ molecules at the interphase, this peak is an indicator of the extent of confinement. The fact that this confinement peak is enhanced in the presence of Mg^{2+} or Ca^{2+} suggests that in the presence of these foreign cations, the hydrophobic layered structure seen at positive potentials with LiTFSI WiSE without additional cations is maintained. In contrast, this layered structure must be altered or removed in the presence of Zn^{2+} or Al^{3+}.

There are additional differences between the behavior of the WiSE alone and that of the WiSE in the presence of Zn^{2+} or Al^{3+}. In particular, the peak maximum for confined $Fe(CN)_6^{4-}$ decreases in both cases potential relative to E_0. The decrease in the potential of the oxidative peak relative to E_0 when $Zn(TFSI)_2$ is present is attributed to the consumption of confined $Fe(CN)_6^{4-}$ at this concentration occurring at lower potentials. From 1.25 to 1.5 mM $Zn(TFSI)_2$, where the shift is most prominent, the density of adsorbed $Fe(CN)_6^{4-}$ molecules falls below that of a single monolayer. Thus, the consumption of diffusion-restricted $Fe(CN)_6^{4-}$ molecules generated on the cathodic sweep may occur before the CV reaches the steady-state current region. An additional factor in the potential shift may be the differing interactions of the solvating cation with the foreign cation. The solvation energy of the cation can cause a shift in the redox potential of an electroactive anion.[57,58] Changes to the dielectric strength and desolvation penalty as foreign cations are added to the electrolyte could also impact the magnitude of the desolvation penalty as $Fe(CN)_6^{4-}$ is oxidized, impacting the oxidation potential of the reduced species.

The presence of Mg^{2+} or Ca^{2+} also results in a change in the confinement peak potential. Contrary to the Zn^{2+} or Al^{3+} cases, the peak potential increases with an increasing multivalent cation concentration in these cases. The addition of both $Ca(TFSI)_2$ and $Mg(TFSI)_2$ result in confinement peaks that indicate the presence of multiple monolayers of $Fe(CN)_6^{4-}$, resulting in an additive effect that shifts confinement peak maxima to more positive potentials.

In addition to the presence and potential of the confinement peak, the addition of all the multivalent cations considered resulted in small decreases to D_O, likely associated with increased viscosity of the WiSE.[59] The addition of Mg^{2+} or Ca^{2+} resulted in a k^0 virtually unchanged compared with the WiSE alone. Alternatively, the addition of Zn or Al resulted in a drop in k^0 from 0.005 cm s^{-1} to 0.002 cm s^{-1} (Zn^{2+}) or from 0.004 to 0.001 (Al^{3+}). The large decreases in k^0 may be due to the occupation or blocking of electrochemical active sites on the electrode surface by hydrated Zn^{2+} or Al^{3+} species. This would reduce the electroactive surface area of the electrode, resulting in an apparent reduction in k^0.

4.2. Potential-Dependent SEIRAS of the $Fe(CN)_6^{3-/4-}$ Redox Couple in WiSE. Spectroscopic investigation of the ν(CN) peak of $Fe(CN)_6^{4-}$ provides additional evidence for the presence of confined $Fe(CN)_6^{4-}$ in the LiTFSI WiSE and its absence when 1.75 mM Zn^{2+} is present. In the LiTFSI WiSE, continued accumulation of $Fe(CN)_6^{4-}$ after the beginning of the reverse potential sweep from 0.1 to 0.2 V vs Ag/Ag^+ is evidence that this species is unable to freely diffuse back into the bulk solution. When 1.75 mM $Zn(TFSI)_2$ is added to the solution, there is a smaller window of accumulation of $Fe(CN)_6^{4-}$ that ends at 0.15 V.

4.3. SEIRAS with Foreign Cations. In the 20 m LiTFSI WiSE, water and $TFSI^-$ exhibit inverse potential dependencies in SEIRAS. Water modes increase and $TFSI^-$ modes decrease in intensity upon application of negative potentials, a result consistent with a previous study at 21 m LiTFSI.[11] This behavior was attributed to the displacement of hydrophobic $TFSI^-$ and $[Li(H_2O)_x]^+([TFSI]^-)_y$ clusters with incoming $[Li(H_2O)_x]^+$ species at negative potentials.[11] The inverse potential-dependent correlation between water and anion is still observed when 1 m $Ca(TFSI)_2$ or 0.5 m $Mg(TFSI)_2$ is added to the WiSE, behavior that is "Li-like", suggesting that neither Ca^{2+} nor Mg^{2+} disrupt the $[Li(H_2O)_x]^+([TFSI]^-)_y$ layers. Upon the addition of 1 m $Zn(TFSI)_2$ to 20 m LiTFSI WiSE, however, all observed FTIR modes assigned to both water and $TFSI^-$ increase with the potential. The same trends were observed in a WiSE consisting of 0.1 m $Al(TFSI)_3$ and 15 m LiTFSI, behavior that is "Zn-like". Thus, the addition of Zn^{2+} or Al^{3+} must disrupt the hydrophobic $TFSI^-$ layer that forms at positive potentials for Li-like electrolytes.

To explain the origin of the voltammetric and spectroscopic behavior seen with addition of cations to the WiSE, we use the differing pK_a values of the cations as a measure of the strength of association to water for each cation. Table 2 provides these different pK_a values. Interestingly, both Zn^{2+} and Al^{3+} (Zn-like cations) exhibit a pK_a value much lower than that of Li^+, while Ca^{2+} and Mg^{2+} (Li-like cations) have pK_a values higher than that of Zn^{2+} and closer to that of Li^+. The lower pK_a of Zn^{2+} and Al^{3+} indicate that water within metal-aqua complexes with

Table 2. pK_a Values of Cations in Electrolyte

cation	pK_a	classification of WiSE with cation addition
Li^+	13.8[60]	Li-like
Ca^{2+}	12.8[61]	Li-like
Mg^{2+}	11.4[61]	Li-like
Zn^{2+}	9.0[61]	Zn-like
Al^{3+}	5.5[62]	Zn-like

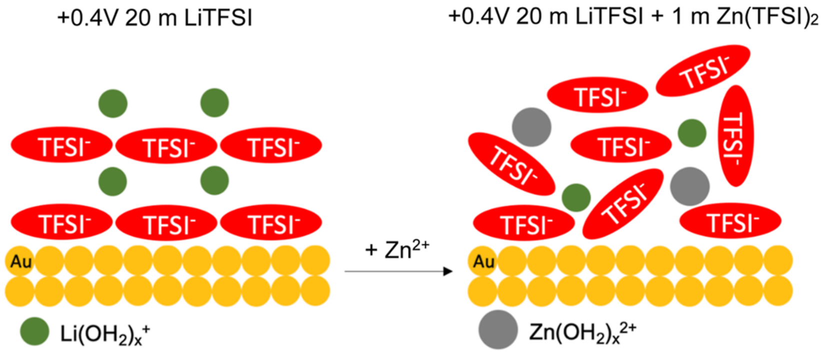

Figure 8. (Left) representation of the interphase at a positively polarized metal surface in the LiTFSI WiSE. (Right) representation of the interphase at a positively polarized metal surface in LiTFSI + $Zn(TFSI)_2$ WiSE.

these cations is bound stronger to the cation compared to Li^+, Ca^{2+}, and Mg^{2+}.[60] We posit that strong cation binding with water disrupts the network of anions at the interphase of some WiSEs. This disruption manifests in the variety of differences observed at the interphases of WiSE with and without a low pK_a cation.

We also note that the Hofmeister series contextualizes the differences in behavior between the cations observed experimentally. Al^{3+} and Zn^{2+}, both considered chaotropes, or water structure breakers, promote the binding of water to the cation. Li^+, Mg^{2+}, and Ca^{2+}, are closer to the water structure forming, or kosmotrope side of the Hofmeister series.[63] This series is also a reflection of the stronger binding of water to Zn^{2+} and Al^{3+}, contributing to the breakdown of the water-TFSI-cation network at the interphase.

As established, SEIRAS in the presence of Zn^{2+} and Al^{3+} (Zn-like cations) indicate that when $TFSI^-$ associates with a positively polarized metal electrode, water is also associated with this interphase. Some of this water, however, likely exists within the solvation shell of the Zn^{2+} cation due to the low pK_a of Zn^{2+} compared to Li^+.

Due to the extreme concentration of LiTFSI WiSE, Li^+ cations tend to exist as dimers or trimers bridged by other species in solution.[18] NMR studies suggested that bridging deprotonated −OH− binding at least two Li^+ molecules plays an important role in the formation of multimeric structures in the bulk.[13] We suggest that higher order negatively charged aggregates containing cations, $TFSI^-$, and water are prevented from forming at the electrode interphase at positive potentials when a cation with a low pK_a is introduced to solution. Thus, low pK_a is associated with a disruptive effect at the interphase, possibly because the high affinity of low pK_a cations for water removes water from $TFSI^-$-rich structures at the interphase. Such an effect would explain UME voltammetry results, as $Fe(CN)_6^{4-}$ could more easily diffuse through a disordered double layer and SEIRAS results, as water removed from its place in an anion-rich interfacial layer may be more visible to SEIRAS.

The disruptive effect associated with Zn-like cation addition is not observed when the added cation does not have a low pK_a. In these cases, including Mg^{2+} or Ca^{2+}, the weaker association between the cation and water prevents a change in the interfacial water structure and preserves the hydrophobic $TFSI^-$ layer. Thus, these Li-like cations exhibit the same trends spectroscopically and electrochemically as those found for the LiTFSI WiSE alone.

Figure 8 shows a cartoon describing the interphase at a positively polarized surface in the presence and absence of Zn^{2+}.

4.4. $TFSI^-$ Vibrational Modes.

We next discuss $TFSI^-$ vibrational modes in the presence of different cations. For the LiTFSI WiSE, the two strongest $TFSI^-$ modes (e and g in this work) increase in intensity at positive potentials and decrease in intensity at negative potentials. Not all $TFSI^-$ associated modes exhibit this behavior, however, while modes e and g increase in intensity at positive potentials, modes a-f do not. In contrast, in the presence of $Zn(TFSI)_2$, all observed $TFSI^-$ associated bands increase in intensity with potential. This same behavior is found in the case of $Al(TFSI)_3$ addition, as shown in Figure S3.

There is substantial work examining $TFSI^-$ modes in different environments. In the low energy region between 700 and 800 cm^{-1}, clear differences in $TFSI^-$ spectroscopy are related to the extent of ion pairing in the electrolyte.[64,65] In the high energy region (1000−1400 cm^{-1}), IR modes are complicated combinations of different atomic displacements, and their behavior is less diagnostic. Different intensities of the bands in this region have been associated with (a) different conformers of $TFSI^-$ (cisoid vs transoid),[41,65−67] (b) different coordination environments,[38,41,67,68] and (related) (c) different concentrations.[20]

In the LiTFSI WiSE + $Zn(TFSI)_2$, nearly all of the $TFSI^-$ associated bands are observed. Particularly, in the region of the out-of-plane and in-plane asymmetric SO_2 stretches (peaks e and g) between 1300 and 1400 cm^{-1}, three peaks appear despite only two bands being present at that location. The third appears as a shoulder of peak g. The presence of this peak is an indication of a mix of cisoid and transoid conformers at the interphase, as there is a slight shift in the energy of the SO_2 bands between the two conformers. In general, the presence of a diversity of bands suggests $TFSI^-$ disorder at the LiTFSI WiSE + $Zn(TFSI)_2$ interphase. This inferred disorder is consistent with the inferences from the UME measurements, where the confining layered structure is removed in the presence of Zn^{2+}.

In contrast to the LiTFSI WiSE + $Zn(TFSI)_2$ case, in the LiTFSI WiSE, not all of the $TFSI^-$ bands are observed. The change in intensity of the different $TFSI^-$ modes may be a consequence of ordering at the interphase, which makes only some of the $TFSI^-$ modes IR allowed. Research suggests that when $TFSI^-$ is coordinated at only one of its two available SO_2 sites, it exhibits a high degree of mobility in the other, uncoordinated SO_2CF_3 group of the molecule.[69] Other work has established that in a LiTFSI-containing WiSE at a positively polarized surface, TFSI$^-$ will adsorb parallel to the surface, coordinating both the positive surface below and the Li$^+$ cations above.[26,68] To coordinate both, the TFSI$^-$ anion must be in the transoid conformation to enable one coordinating SO$_2$ group to point down to coordinate the surface and the other to point up to coordinate the cation. This conformational selection at the interphase may be the origin of the limited number of TFSI$^-$ modes in the interphase. A detailed understanding of the spectroscopy in this region, however, will require the use of single crystals and polarization techniques.

4.5. AFM Experiments. The AFM data reported above reveal that the addition of Zn^{2+} to LiTFSI WiSE results in a disruption of the WiSE clustering structure observed for 21 m LiTFSI WiSE and 20 m LiTFSI + 0.1 m Ca(TFSI)$_2$ WiSE. The structure of the EDL for the 20 m LiTFSI + 1 m Zn(TFSI)$_2$ exhibits a number of differences from 20 m LiTFSI + 0.1 m Ca(TFSI)$_2$ and 21 m LiTFSI WiSE. While the introduction of the Ca^{2+} ion to the WiSE promotes greater heterogeneity at the interphase, the presence of only two layers at negative bias in the Zn^{2+} case, in contrast to Ca^{2+} or LiTFSI alone, reflects the more significant disruption of the interfacial structure by Zn^{2+}. Additionally, at negative bias, AFM results for 20 m LiTFSI + 1 m Zn(TFSI)$_2$ WiSE showed the presence of a large layer with a large error in size, presumably a combination of strongly hydrated [Zn(H$_2$O)$_x$]$^{2+}$ and clusters of cations with TFSI$^-$. These large layers were observed only in the Zn^{2+} case, indicating that the interaction between Zn^{2+} and TFSI$^-$ at the interphase is strong, possibly contributing to the disruption of the interaction between Li$^+$ and TFSI$^-$ that is present in the neat WiSE. The presence of anion−cation clusters also indicates the applied potential is greatly screened by the surface-adsorbed layers (Zn^{2+}), which is consistent with the reduction of k^0 for Fe(CN)$_6^{3-/4-}$ upon Zn^{2+} addition to LiTFSI WiSE. The larger thickness of the layer could also reflecting a weaker electrostatic attraction to the Au surface.

At positive bias, only two layers were observed for 20 m LiTFSI + 1 m Zn(TFSI)$_2$ WiSE, in contrast to 20 m LiTFSI + 0.1 m Ca(TFSI)$_2$ or 21 m LiTFSI. Overall, Zn^{2+} seems to hinder large clusters from approaching the positive Au surface, thereby reducing both the extent of overscreening (co-ions) and the presence of clusters close to the positive Au surface. This inhibition of cluster approach might be because Zn^{2+} interacts strongly with water as indicated by low pK_a, and disrupts the WiSE structure, i.e., the coordination between Li$^+$ with TFSI$^-$ anions and water—at least close to the surface. This modified EDL might also justify the disruption of the confinement effect of the redox species. Overall, these results support the conclusions drawn from UME and SEIRAS experiments that resulted in the classification of Ca^{2+} as a "Li-like" cation, and Zn^{2+} in a separate category of "Zn-like" cations.

5. CONCLUSIONS

We demonstrate that the potential-dependent layered structure of the metal/WiSE interphase of 20 m LiTFSI is altered by the presence of multivalent cations and that this effect is correlated to the strength of the metal-aqua complex, as measured by cation pK_a and also correlated with the place of the cation on the Hofmeister series. SEIRAS and AFM results indicate that in WiSE without multivalent cation, or when the multivalent cation does not have a sufficiently low pK_a or chaotropicity (Mg^{2+} and Ca^{2+}), the double-layer structure exhibits a potential-dependent enhancement of water at negative potentials and TFSI$^-$ and cluster-containing TFSI$^-$, water, and cation at positive potentials. This double-layer structure results in the confinement of Fe(CN)$_6^{4-}$ at the interphase. However, the presence of low pK_a or chaotropic cations (Zn^{2+} and Al^{3+}) results in a disordered interphase and the removal of the confinement effect. At positive potentials, clusters are not observed in AFM, and SEIRAS results show an enhancement of water. This work shows that cations with a high affinity for water disrupt the ordered interphase present in the LiTFSI WiSE, which highlights the important contribution of water as a bridge in layered structures at the interphase.

ASSOCIATED CONTENT

Supporting Information

The Supporting Information is available free of charge at https://pubs.acs.org/doi/10.1021/acsaem.4c00507.

Al(TFSI)$_3$ characterization, additional Zn(TFSI)$_2$-containing WiSE SEIRAS, additional Al(TFSI)$_3$-containing WiSE SEIRAS, AFM force−separation curves and heatmaps for Zn(TFSI)$_2$-containing WiSE, and AFM force−separation curves and heatmaps for Ca(TFSI)$_2$-containing WiSE (PDF)

AUTHOR INFORMATION

Corresponding Author

Andrew A. Gewirth − *Department of Chemistry, University of Illinois at Urbana−Champaign, Urbana, Illinois 61801, United States; Frederick Seitz Materials Research Laboratory, University of Illinois at Urbana−Champaign, Urbana, Illinois 61801, United States;* orcid.org/0000-0003-4400-9907; Phone: +1-217-333-8329; Email: agewirth@illinois.edu

Authors

Alexis G. Hoane − *Department of Chemistry, University of Illinois at Urbana−Champaign, Urbana, Illinois 61801, United States;* orcid.org/0009-0002-4488-8841

Qianlu Zheng − *Department of Civil and Environmental Engineering, University of Illinois at Urbana−Champaign, Urbana, Illinois 61801, United States*

Nicholas D. Maldonado − *Department of Chemistry, University of Illinois at Urbana−Champaign, Urbana, Illinois 61801, United States*

Rosa M. Espinosa-Marzal − *Department of Civil and Environmental Engineering and Department of Materials Science and Engineering, University of Illinois at Urbana−Champaign, Urbana, Illinois 61801, United States;* orcid.org/0000-0003-3442-2511

Complete contact information is available at: https://pubs.acs.org/10.1021/acsaem.4c00507

Notes

The authors declare no competing financial interest.

ACKNOWLEDGMENTS

This work was supported as part of the Joint Center for Energy Storage Research (JCESR), an Energy Innovation Hub funded by the U.S. Department of Energy, Office of Science, Basic Energy Sciences. A.G.H. acknowledges support from the Lester E. and Kathleen A. Coleman Fellowship Fund. We thank machine shop from the School of Chemical Sciences for SEIRAS spectro-electrochemical cell fabrication. Materials for SEIRAS were prepared in part in the Frederick Seitz Materials Research Laboratory, Central Research Facilities, University of Illinois. We thank Heryn K. Wang for the NMR characterization. Q.Z. and R.M.E.-M. gratefully acknowledge the financial support from the National Science Foundation under grant DMR-1904681.

■ REFERENCES

(1) Goodenough, J. B.; Park, K.-S. The Li-Ion Rechargeable Battery: A Perspective. *J. Am. Chem. Soc.* **2013**, *135* (4), 1167−1176.

(2) Manthiram, A. Materials Challenges and Opportunities of Lithium Ion Batteries. *J. Phys. Chem. Lett.* **2011**, *2* (3), 176−184.

(3) Zubi, G.; Dufo-López, R.; Carvalho, M.; Pasaoglu, G. The lithium-ion battery: State of the art and future perspectives. *Renewable Sustainable Energy Rev.* **2018**, *89*, 292−308.

(4) Liang, Y.; Dong, H.; Aurbach, D.; Yao, Y. Current status and future directions of multivalent metal-ion batteries. *Nat. Energy* **2020**, *5* (9), 646−656.

(5) Blanc, L. E.; Kundu, D.; Nazar, L. F. Scientific Challenges for the Implementation of Zn-Ion Batteries. *Joule* **2020**, *4* (4), 771−799.

(6) Yi, Z.; Chen, G.; Hou, F.; Wang, L.; Liang, J. Strategies for the stabilization of Zn metal anodes for Zn-ion batteries. *Adv. Energy Mater.* **2021**, *11* (1), 2003065.

(7) Khan, Z.; Kumar, D.; Crispin, X. Does Water-in-Salt Electrolyte Subdue Issues of Zn Batteries? *Adv. Mater.* **2023**, *35* (36), 2300369.

(8) Suo, L.; Borodin, O.; Gao, T.; Olguin, M.; Ho, J.; Fan, X.; Luo, C.; Wang, C.; Xu, K. Water-in-salt" electrolyte enables high-voltage aqueous lithium-ion chemistries. *Science* **2015**, *350* (6263), 938−943.

(9) Li, Z.; Bouchal, R.; Mendez-Morales, T.; Rollet, A. L.; Rizzi, C.; Le Vot, S.; Favier, F.; Rotenberg, B.; Borodin, O.; Fontaine, O.; Salanne, M. Transport Properties of Li-TFSI Water-in-Salt Electrolytes. *J. Phys. Chem. B* **2019**, *123* (49), 10514−10521.

(10) McEldrew, M.; Goodwin, Z. A. H.; Kornyshev, A. A.; Bazant, M. Z. Theory of the Double Layer in Water-in-Salt Electrolytes. *J. Phys. Chem. Lett.* **2018**, *9* (19), 5840−5846.

(11) Zhang, R.; Han, M.; Ta, K.; Madsen, K. E.; Chen, X.; Zhang, X.; Espinosa-Marzal, R. M.; Gewirth, A. A. Potential-Dependent Layering in the Electrochemical Double Layer of Water-in-Salt Electrolytes. *ACS Appl. Energy Mater.* **2020**, *3* (8), 8086−8094.

(12) Han, M.; Zhang, R.; Gewirth, A. A.; Espinosa-Marzal, R. M. Nanoheterogeneity of LiTFSI Solutions Transitions Close to a Surface and with Concentration. *Nano Lett.* **2021**, *21* (5), 2304−2309.

(13) Han, K. S.; Yu, Z.; Wang, H.; Redfern, P. C.; Ma, L.; Cheng, L.; Chen, Y.; Hu, J. Z.; Curtiss, L. A.; Xu, K.; Murugesan, V.; Mueller, K. T. Origin of Unusual Acidity and Li+ Diffusivity in a Series of Water-in-Salt Electrolytes. *J. Phys. Chem. B* **2020**, *124* (25), 5284−5291.

(14) Maffre, M.; Bouchal, R.; Freunberger, S. A.; Lindahl, N.; Johansson, P.; Favier, F.; Fontaine, O.; Bélanger, D. Investigation of electrochemical and chemical processes occurring at positive potentials in "water-in-salt" electrolytes. *J. Electrochem. Soc.* **2021**, *168* (5), 050550.

(15) Shen, Y.; Liu, B.; Liu, X.; Liu, J.; Ding, J.; Zhong, C.; Hu, W. Water-in-salt electrolyte for safe and high-energy aqueous battery. *Energy Storage Mater.* **2021**, *34*, 461−474.

(16) Lim, J.; Park, K.; Lee, H.; Kim, J.; Kwak, K.; Cho, M. Nanometric Water Channels in Water-in-Salt Lithium Ion Battery Electrolyte. *J. Am. Chem. Soc.* **2018**, *140* (46), 15661−15667.

(17) Zhang, M.; Hao, H.; Zhou, D.; Duan, Y.; Wang, Y.; Bian, H. Understanding the Microscopic Structure of a "Water-in-Salt" Lithium Ion Battery Electrolyte Probed with Ultrafast IR Spectroscopy. *J. Phys. Chem. C* **2020**, *124* (16), 8594−8604.

(18) Borodin, O.; Suo, L.; Gobet, M.; Ren, X.; Wang, F.; Faraone, A.; Peng, J.; Olguin, M.; Schroeder, M.; Ding, M. S.; Gobrogge, E.; von Wald Cresce, A.; Munoz, S.; Dura, J. A.; Greenbaum, S.; Wang, C.; Xu, K. Liquid Structure with Nano-Heterogeneity Promotes Cationic Transport in Concentrated Electrolytes. *ACS Nano* **2017**, *11* (10), 10462−10471.

(19) Wang, F.; Borodin, O.; Gao, T.; Fan, X.; Sun, W.; Han, F.; Faraone, A.; Dura, J. A.; Xu, K.; Wang, C. Highly reversible zinc metal anode for aqueous batteries. *Nat. Mater.* **2018**, *17* (6), 543−549.

(20) Zhang, Y.; Wan, G.; Lewis, N. H. C.; Mars, J.; Bone, S. E.; Steinrück, H. G.; Lukatskaya, M. R.; Weadock, N. J.; Bajdich, M.; Borodin, O.; Tokmakoff, A.; Toney, M. F.; Maginn, E. J. Water or Anion? Uncovering the Zn2+ Solvation Environment in Mixed Zn(TFSI)2 and LiTFSI Water-in-Salt Electrolytes. *ACS Energy Lett.* **2021**, *6* (10), 3458−3463.

(21) Boyle, D. T.; Kong, X.; Pei, A.; Rudnicki, P. E.; Shi, F.; Huang, W.; Bao, Z.; Qin, J.; Cui, Y. Transient Voltammetry with Ultramicroelectrodes Reveals the Electron Transfer Kinetics of Lithium Metal Anodes. *ACS Energy Lett.* **2020**, *5* (3), 701−709.

(22) Ta, K.; See, K. A.; Gewirth, A. A. Elucidating Zn and Mg Electrodeposition Mechanisms in Nonaqueous Electrolytes for Next-Generation Metal Batteries. *J. Phys. Chem. C* **2018**, *122* (25), 13790−13796.

(23) Kozuch, J.; Ataka, K.; Heberle, J. Surface-enhanced infrared absorption spectroscopy. *Nat. Rev. Methods Primers* **2023**, *3* (1), 70.

(24) Osawa, M. In-situ surface-enhanced infrared spectroscopy of the electrode/solution interface. *Adv. Electrochem. Sci. Eng.: Diffr. Spectrosc. Methods Electrochem.* **2006**, *9*, 269−314.

(25) Ataka, K.-i.; Yotsuyanagi, T.; Osawa, M. Potential-Dependent Reorientation of Water Molecules at an Electrode/Electrolyte Interface Studied by Surface-Enhanced Infrared Absorption Spectroscopy. *J. Phys. Chem. A* **1996**, *100* (25), 10664−10672.

(26) Borodin, O.; Ren, X.; Vatamanu, J.; von Wald Cresce, A.; Knap, J.; Xu, K. Modeling Insight into Battery Electrolyte Electrochemical Stability and Interfacial Structure. *Acc. Chem. Res.* **2017**, *50* (12), 2886−2894.

(27) Zheng, Q.; Goodwin, Z. A. H.; Gopalakrishnan, V.; Hoane, A. G.; Han, M.; Zhang, R.; Hawthorne, N.; Batteas, J. D.; Gewirth, A. A.; Espinosa-Marzal, R. M. Water in the Electrical Double Layer of Ionic Liquids on Graphene. *ACS Nano* **2023**, *17* (10), 9347−9360.

(28) Oldiges, K.; von Aspern, N.; Cekic-Laskovic, I.; Winter, M.; Brunklaus, G. Impact of trifluoromethylation of adiponitrile on aluminum dissolution behavior in dinitrile-based electrolytes. *J. Electrochem. Soc.* **2018**, *165* (16), A3773−A3781.

(29) Morhart, T. A.; Unni, B.; Lardner, M. J.; Burgess, I. J. Electrochemical ATR-SEIRAS Using Low-Cost, Micromachined Si Wafers. *Anal. Chem.* **2017**, *89* (21), 11818−11824.

(30) Nogues, C.; Wanunu, M. A rapid approach to reproducible, atomically flat gold films on mica. *Surf. Sci.* **2004**, *573* (3), L383−L389.

(31) Atkin, R.; Warr, G. G. Structure in Confined Room-Temperature Ionic Liquids. *J. Phys. Chem. C* **2007**, *111* (13), 5162−5168.

(32) Bard, A. J.; Faulkner, L. R. *Electrochemical Methods Fundamentals and Applications*; John Wiley and Sons, Inc, 2001.

(33) Zheng, Q.; Shao, H. Correlation between redox species adsorption and electron transfer kinetics of mildly oxidized graphene: A chronocoulometry and SECM study. *Electrochem. Commun.* **2019**, *103*, 83−87.

(34) Salazar-Banda, G. R.; Eguiluz, K. I. B.; Carvalho, A. E. d.; Avaca, L. A. Ultramicroelectrode Array Behavior of Electrochemically Partially Blocked Boron-Doped Diamond Surface. *J. Braz. Chem. Soc.* **2013**.

(35) Szulborska, A.; Baranski, A. Kinetics and thermodynamics of thioglycol adsorption on mercury ultramicroelectrodes. *J. Electroanal. Chem.* **1994**, *377* (1−2), 269−281.

(36) Brown, D. B.; Shriver, D. F. Structures and solid-state reactions of Prussian blue analogs containing chromium, manganese, iron, and cobalt. *Inorg. Chem.* **1969**, *8* (1), 37−42.

(37) Pharr, C. M.; Griffiths, P. R. Infrared Spectroelectrochemical Analysis of Adsorbed Hexacyanoferrate Species Formed during Potential Cycling in the Ferrocyanide/Ferricyanide Redox Couple. *Anal. Chem.* **1997**, *69* (22), 4673−4679.

(38) Rey, I.; Johansson, P.; Lindgren, J.; Lassègues, J. C.; Grondin, J.; Servant, L. Spectroscopic and Theoretical Study of (CF3SO2)2N-(TFSI-) and (CF3SO2)2NH (HTFSI). *J. Phys. Chem. A* **1998**, *102* (19), 3249−3258.

(39) Seki, T.; Chiang, K.-Y.; Yu, C.-C.; Yu, X.; Okuno, M.; Hunger, J.; Nagata, Y.; Bonn, M. The Bending Mode of Water: A Powerful Probe for Hydrogen Bond Structure of Aqueous Systems. *J. Phys. Chem. Lett.* **2020**, *11* (19), 8459−8469.

(40) Lewis, N. H. C.; Zhang, Y.; Dereka, B.; Carino, E. V.; Maginn, E. J.; Tokmakoff, A. Signatures of Ion Pairing and Aggregation in the Vibrational Spectroscopy of Super-Concentrated Aqueous Lithium Bistriflimide Solutions. *J. Phys. Chem. C* **2020**, *124* (6), 3470−3481.

(41) Rey, I.; Lassègues, J.; Grondin, J.; Servant, L. Infrared and Raman study of the PEO-LiTFSI polymer electrolyte. *Electrochim. Acta* **1998**, *43* (10−11), 1505−1510.

(42) Petit, T.; Puskar, L.; Dolenko, T.; Choudhury, S.; Ritter, E.; Burikov, S.; Laptinskiy, K.; Brzustowski, Q.; Schade, U.; Yuzawa, H.; Nagasaka, M.; Kosugi, N.; Kurzyp, M.; Venerosy, A.; Girard, H.; Arnault, J.-C.; Osawa, E.; Nunn, N.; Shenderova, O.; Aziz, E. F. Unusual Water Hydrogen Bond Network around Hydrogenated Nanodiamonds. *J. Phys. Chem. C* **2017**, *121* (9), 5185−5194.

(43) Bazant, M. Z.; Storey, B. D.; Kornyshev, A. A. Double Layer in Ionic Liquids: Overscreening versus Crowding. *Phys. Rev. Lett.* **2011**, *106* (4), 046102.

(44) Israelachvili, J. N. *Intermolecular and Surface Forces*, 3rd ed.; Elsevier Science, 2011; .

(45) Heuberger, M.; Zäch, M. Nanofluidics: structural forces, density anomalies, and the pivotal role of nanoparticles. *Langmuir* **2003**, *19* (6), 1943−1947.

(46) Lee, S. S.; Fenter, P.; Nagy, K. L.; Sturchio, N. C. Monovalent ion adsorption at the muscovite (001)-solution interface: Relationships among ion coverage and speciation, interfacial water structure, and substrate relaxation. *Langmuir* **2012**, *28* (23), 8637−8650.

(47) Zachariah, Z.; Espinosa-Marzal, R. M.; Spencer, N. D.; Heuberger, M. P. Stepwise Collapse of Highly Overlapping Electrical Double Layers. *Phys. Chem. Chem. Phys.* **2016**, *18*, 24417−24427. 10.1039/C6CP04222H

(48) Cook, A.; Ueno, K.; Watanabe, M.; Atkin, R.; Li, H. Effect of Variation in Anion Type and Glyme Length on the Nanostructure of the Solvate Ionic Liquid/Graphite Interface as a Function of Potential. *J. Phys. Chem. C* **2017**, *121*, 15728−15734.

(49) McLean, B.; Li, H.; Stefanovic, R.; Wood, R. J.; Webber, G. B.; Ueno, K.; Watanabe, M.; Warr, G. G.; Page, A.; Atkin, R. Nanostructure of [Li(G_4)]TFSI and [Li(G_4)]NO_3 Solvate Ionic Liquids at HOPG and Au(111) Electrode Interfaces as a Function of Potential. *Phys. Chem. Chem. Phys.* **2015**, *17*, 325−333.

(50) Carstens, T.; Gustus, R.; Höfft, O.; Borisenko, N.; Endres, F.; Li, H.; Wood, R. J.; Page, A. J.; Atkin, R. Combined STM, AFM, and DFT Study of the Highly Ordered Pyrolytic Graphite/1-Octyl-3-methyl-imidazolium Bis(trifluoromethylsulfonyl)imide Interface. *J. Phys. Chem. C* **2014**, *118*, 10833−10843.

(51) McEwen, A. B.; Ngo, H. L.; LeCompte, K.; Goldman, J. L. Electrochemical Properties of Imidazolium Salt Electrolytes for Electrochemical Capacitor Applications. *J. Electrochem. Soc.* **1999**, *146*, 1687−1695.

(52) Zhong, C.; Deng, Y.; Hu, W.; Qiao, J.; Zhang, L.; Zhang, J. A review of electrolyte materials and compositions for electrochemical supercapacitors. *Chem. Soc. Rev.* **2015**, *44* (21), 7484−7539. 10.1039/C5CS00303B

(53) Goodwin, Z. A. H.; Kornyshev, A. A. Cracking Ion Pairs in the Electrical Double Layer of Ionic Liquids. *Electrochim. Acta* **2022**, *434*, 141163.

(54) Goodwin, Z. A. H.; McEldrew, M.; Pedro de Souza, J.; Bazant, M. Z.; Kornyshev, A. A. Gelation, clustering, and crowding in the electrical double layer of ionic liquids. *J. Chem. Phys.* **2022**, *157* (9), 094106.

(55) Tivony, R.; Klein, J. Probing the Surface Properties of Gold at Low Electrolyte Concentration. *Langmuir* **2016**, *32* (29), 7346−7355.

(56) Kumal, R. R.; Karam, T. E.; Haber, L. H. Determination of the Surface Charge Density of Colloidal Gold Nanoparticles Using Second Harmonic Generation. *J. Phys. Chem. C* **2015**, *119* (28), 16200−16207.

(57) Zhao, Y.; Yu, Z.; Robertson, L. A.; Zhang, J.; Shi, Z.; Bheemireddy, S. R.; Shkrob, I. A.; Y, Z.; Li, T.; Zhang, Z.; Cheng, L.; Zhang, L. Unexpected electrochemical behavior of an anolyte redoxmer in flow battery electrolytes: solvating cations help to fight against the thermodynamic-kinetic dilemma. *J. Mater. Chem. A* **2020**, *8* (27), 13470−13479.

(58) Nikitina, V. A.; Gruber, F.; Jansen, M.; Tsirlina, G. A. Subsequent redox transitions as a tool to understand solvation in ionic liquids. *Electrochim. Acta* **2013**, *103*, 243−251.

(59) Yamada, Y.; Yamada, A. Review—Superconcentrated Electrolytes for Lithium Batteries. *J. Electrochem. Soc.* **2015**, *162* (14), A2406−A2423.

(60) Kumar, A.; Blakemore, J. D. On the Use of Aqueous Metal-Aqua pKa Values as a Descriptor of Lewis Acidity. *Inorg. Chem.* **2021**, *60* (2), 1107−1115.

(61) Jackson, V. E.; Felmy, A. R.; Dixon, D. A. Prediction of the pKa's of Aqueous Metal Ion + 2 Complexes. *J. Phys. Chem. A* **2015**, *119* (12), 2926−2939.

(62) Sigel, H.; Sigel, A. *Metal Ions in Biological Systems Vol. 24 Aluminum and its Role in Biology*; Marcel Dekker, Inc., 1988.

(63) Gregory, K. P.; Elliott, G. R.; Robertson, H.; Kumar, A.; Wanless, E. J.; Webber, G. B.; Craig, V. S.; Andersson, G. G.; Page, A. J. Understanding specific ion effects and the Hofmeister series. *Phys. Chem. Chem. Phys.* **2022**, *24* (21), 12682−12718.

(64) Bakker, A.; Gejji, S.; Lindgren, J.; Hermansson, K.; Probst, M. M. Contact ion pair formation and ether oxygen coordination in the polymer electrolytes M[N(CF3SO2)2]2PEOn for M = Mg, Ca, Sr and Ba. *Polymer* **1995**, *36* (23), 4371−4378.

(65) Martinelli, A.; Matic, A.; Johansson, P.; Jacobsson, P.; Börjesson, L.; Fernicola, A.; Panero, S.; Scrosati, B.; Ohno, H. Conformational evolution of TFSI- in protic and aprotic ionic liquids. *J. Raman Spectrosc.* **2011**, *42* (3), 522−528.

(66) Fujii, K.; Seki, S.; Fukuda, S.; Kanzaki, R.; Takamuku, T.; Umebayashi, Y.; Ishiguro, S.-i. Anion Conformation of Low-Viscosity Room-Temperature Ionic Liquid 1-Ethyl-3-methylimidazolium Bis(fluorosulfonyl) Imide. *J. Phys. Chem. B* **2007**, *111* (44), 12829−12833.

(67) Malaspina, T.; Colherinhas, G.; Weitzner, S. E.; Wood, B. C.; Eterno Fileti, E. Unraveling local structures of Salt-in-Water and Water-in-Salt electrolytes via ab initio molecular dynamics. *J. Mol. Liq.* **2023**, *383*, 122097.

(68) Vatamanu, J.; Borodin, O. Ramifications of Water-in-Salt Interfacial Structure at Charged Electrodes for Electrolyte Electrochemical Stability. *J. Phys. Chem. Lett.* **2017**, *8* (18), 4362−4367.

(69) Reber, D.; Takenaka, N.; Kühnel, R. S.; Yamada, A.; Battaglia, C. Impact of Anion Asymmetry on Local Structure and Supercooling Behavior of Water-in-Salt Electrolytes. *J. Phys. Chem. Lett.* **2020**, *11* (12), 4720−4725.